Chemotactic behaviour of *Escherichia coli* at high cell density

Remy Colin[1,2,*], Knut Drescher[1,2,3] and Victor Sourjik[1,2,*]

[1] Max Planck Institute for Terrestrial Microbiology
[2] Loewe Center for Synthetic Microbiology
[3] Fachbereich Physik, Philipps-Universität Marburg
Karl-von-Frisch-Str. 16, 35043 Marburg

October 25, 2019

Abstract

At high cell density, swimming bacteria exhibit collective motility patterns, self-organized through physical interactions of a however still debated nature. Although high-density behaviours are frequent in natural situations, it remained unknown how collective motion affects chemotaxis, the main physiological function of motility, which enables bacteria to follow environmental gradients in their habitats. Here, we systematically investigate this question in the model organism *Escherichia coli*, varying cell density, cell length, and suspension confinement. The characteristics of the collective motion indicate that hydrodynamic interactions between swimmers made the primary contribution to its emergence. We observe that the chemotactic drift is moderately enhanced at intermediate cell densities, peaks, and is then strongly suppressed at higher densities. Numerical simulations reveal that this suppression occurs because the collective motion disturbs the choreography necessary for chemotactic sensing. We suggest that this physical hindrance imposes a fundamental constraint on high-density behaviours of motile bacteria, including swarming and the formation of multicellular aggregates and biofilms.

---

*To whom correspondence should be addressed. E-mail: remy.colin@synmikro.mpi-marburg.mpg.de, victor.sourjik@synmikro.mpi-marburg.mpg.de

Indroduction

When the cell density of a suspension of swimming bacteria increases, collective motion emerges, characterized by intermittent jets and swirls of groups of cells [1–3]. This behaviour is observed for many microorganisms not only in artificial but also in natural situations, often at an interface, e.g. when bacteria swarm on a moist surface in the lab [4–8] or during infection [9], or at an air-water interface during formation of pellicle biofilms [1, 10]. Bacterial collective motion has been extensively studied experimentally [11–14] and theoretically [15–20], and it is known to emerge from the alignment between the self-propelled cells [21]. Two alignment mechanisms have been proposed, based either on steric interactions between the rod-like bacteria [22–24] or on the hydrodynamics of the flow they create as they swim [15, 17], which displays a pusher force dipole flow symmetry [3, 25, 26]. However, the relative importance of these two mechanisms has not been clearly established so far [27].

Bacterial collective motion contrasts to the behaviour of individual motile cells in dilute suspension, when bacteria swim in relatively straight second-long runs interrupted by short reorientations (tumbles), resulting at long times in a random walk by which they explore their environment [28]. Bacteria can furthermore navigate in environmental gradients by biasing this motion pattern: they lengthen (resp. shorten) their runs when swimming toward attractive (resp. repulsive) environment [28]. The biochemical signaling pathway controlling this chemotactic behaviour is well understood in *E. coli* [29, 30] and it is one of the best modeled biological signaling systems [31]. Bacteria monitor – via their chemoreceptors – the changes in environmental conditions and respond to them by modifying a phosphorylation signal transmitted to the flagellar motors to change the tumbling frequency accordingly [32, 33]. In *E. coli*, attractant substances repress the phosphorylation signal, which results in prolonged runs, repellents having the opposite effect. An adaptation module slowly resets the receptor sensitivity for further stimulations, via a negative feedback loop [34, 35]. This effectively allows the cell to compare its current situation to the recent past while swimming along a given direction [30], with a memory timescale of a few seconds [36, 37]. Notably, the rotational Brownian motion of the cell body interferes with this mechanism of sensing by randomly changing the direction of swimming while temporal comparisons are performed [28, 29].

Although typically seen as a single-cell behaviour, chemotaxis also drives collective behaviours based on chemical interactions, such as autoaggregation [38, 39], self-concentration in patches [40, 41] and travelling band formation [42, 43], where the chemotactic response to self-generated gradients of chemoattractants leads to local cell density increases. However, very little is known about how the high-density physical interactions and the resulting collective motion influence the chemotactic navigation of bacteria [44, 45]: for example, it is unclear whether chemotaxis would be improved by alignments of convective flows with the gradient [19, 45] or instead compromised by random collisions between cells. This lack of knowledge is in part due to the technical difficulty of measuring the dynamics of cells in a dense suspension [20]. Over the last few years, new image analysis methods have been developed or adapted to bacterial systems [2, 46–49], which exploit intensity fluctuations [46] or intensity pattern shifts [49] to characterize swimming and chemotaxis in populations of bacteria. These Fourier image analysis methods function at arbitrarily high cell densities, capture the dynamics of all cells without bias, and are at least as fast as the more commonly used particle tracking techniques.

In this paper, we use Fourier image analysis methods to investigate how the collective motion developing with increasing cell density affects the ability of *E. coli* populations to follow controlled chemical gradients in a microdevice. Our experimental results and computer simulations show that, after increasing up to a maximum at intermediate densities, chemotaxis is strongly reduced as collective motion developed in the sample. Collective reorientations act similarly to an active rotational diffusion interfering with the chemosensing mechanism. Additionally, the characteristics of the collective motion are consistent

2

62 with hydrodynamic interactions being the primary driver of its emergence, additional steric effects being
63 important but secondary. These results have important implications for collective behaviours of motile
64 bacteria at high density.

Results

Measuring chemotactic motion at variable cell density

67 To measure both the collective dynamics and the chemotactic response of populations of *E. coli* cells at
68 varying density, we analyzed bacterial swimming in controlled gradients of a chemical attractant using
69 a microfluidics setup, videomicroscopy and Fourier image analysis. Microfabricated devices made of the
70 oxygen-permeable polymer poly-dimethylsiloxane (PDMS) were used as described previously [49] to create
71 quasi-static linear gradients of the non-metabolizable attractant α-methyl-D,L-aspartic acid (MeAsp) in a
72 straight channel (Fig. 1a). This gradient could be mimicked using the fluorescent dye fluorescein (Fig 1b),
73 which has a diffusion coefficient similar to the one of MeAsp ($D \simeq 500\,\mu\mathrm{m}^2/\mathrm{s}$). Three channel heights,
74 $h = 50$, 30 and $8\,\mu\mathrm{m}$, were used to increasingly confine the cell suspensions towards two dimensions.
75 Motility of suspensions of *E. coli* bacteria, measured in the middle of this gradient, was sustained for
76 several hours at all cell densities (Supplementary Fig. 1a), due to oxygen availability and abounding
77 energy source in the medium. When the density increased, the development of collective motion in the
78 sample, characterized by the existence of collective eddies and jets of swimming cells was observed (Fig.
79 2a) as expected [2, 13, 20]. The shape of the gradient, after the transient phase during which it becomes
80 established, is largely unaffected by the collective motion (Fig. 1c), except at the highest bacterial cell
81 body volume fractions. Consistantly, the Peclet number, which compares diffusion and advective transport
82 of MeAsp in an eddy, remains moderate ($Pe = hv_\mathrm{f}/D \leq 1$, where v_f is the fluid velocity; see Supplementary
83 Note 1), confirming that stirring by the bacteria has little effect on the diffusion of MeAsp [50]. Furthermore,
84 in the present geometry, at steady state the gradient shape does not depend on the diffusion coefficient.
85 Because the cell density slowly changes with time in the area of measurement due to the chemotactic
86 accumulation, thus differing from the average cell density in the suspension, the cell body volume fraction
87 Φ_c was measured *in situ* for each experiment (Supplementary Fig. 2 and Methods).

88 To further investigate the effect of cell elongation, which is typically observed for bacteria swarming on
89 a wet hydrogel at high density [4], we compared normally-sized *E. coli* with average length $L = 2\,\mu\mathrm{m}$ and
90 cells elongated to an average of $L = 4\,\mu\mathrm{m}$ upon treatment with cephalexin, a drug preventing cell division
91 (Methods and Supplementary Fig. 2). We observed that the cephalexin treatment strongly increases cell
92 autoaggregation, which is mediated in this *E. coli* strain by the adhesin Antigen 43 [38]. We then used Δflu
93 strain deleted for the gene encoding this adhesin for all results reported in this study, since, in absence of
94 the cephalexin treatment, $flu+$ and Δflu cells behave similarly, regarding both their collective motion and
95 chemotaxis (Supplementary Fig. 3), and the elongated Δflu cells show normal motility (Supplementary
96 Fig. 1).

Structure of the collective motion

98 The collective motion was measured in the gradient using an image velocimetry method derived from
99 Phase Differential Microscopy [49] (Methods) to quantify the local velocity field $\mathbf{v}(\mathbf{r})$, averaged over several
100 neighboring bacteria (Fig. 2a). The spatial structure of the flow field at varying cell volume fraction Φ_c

3

101 was characterized by the 2-dimensional power spectral density of the velocity field (Methods) [20]:

$$E(q) = q \left\langle \frac{\tilde{\mathbf{v}}(\mathbf{q},t)\tilde{\mathbf{v}}^*(\mathbf{q},t)}{A_0 \langle \mathbf{v}^2 \rangle} \right\rangle_{t,|\mathbf{q}|=q}, \tag{1}$$

102 with $\tilde{\mathbf{v}}$ the spatial Fourier transform of $\mathbf{v}$, $\mathbf{q}$ the wave vector and A_0 the area of the field of view. This
103 quantity $E(q)$ (Fig. 2b) measures the distribution of kinetic energy over the flow structure sizes π/q, hence
104 representing the probability to observe a "vortex" of size π/q [20]. At $\Phi_c \gtrsim 0.01$, this flow structure
105 factor exhibits, at a low wave number q_{max}, a maximum $E(q_{max})$, which grows in amplitude as the cell
106 volume fraction increases (Fig. 2b). After an initial decrease, the value of q_{max} reaches a plateau q_{str}
107 at moderate cell volume fraction, corresponding to $E(q_{max}) \gtrsim 15\,\mu\text{m}$ (Supplementary Fig. 4a). Fully
108 developed collective motion thus takes the form of flow structures (eddies) with a specific size, π/q_{str}. An
109 increase in cell density results in an increase of the amount of collective flow of this size – the amplitude
110 of the collective motion, which can be quantified by $E(q_{str})$. Interestingly, q_{str} is apparently determined by
111 the height h of the channel (Fig. 2c inset and Supplementary Fig. 4a), indicating that the flow structures
112 are constrained by the system size. The observed decrease of q_{max} at low cell volume fraction might be due
113 to a combination of $E(q_{max})$ reaching the noise level, represented by the featureless $E(q)$ observed at the
114 lowest cell volume fractions (Fig. 2b), and a genuine reduction of the eddy size when Φ_c becomes low.

115 For simplicity, the amplitude of the collective motion was quantified by $\Delta E(q_{str})$ at all volume fractions
116 (Fig. 2c), i.e. $E(q_{str})$ (Supplementary Fig. 4b, c) corrected for background noise. We observed that
117 $\Delta E(q_{str})$ tends to grow more slowly with volume fraction for more confined suspensions (lower h). At
118 moderate confinement ($h = 30$ and $50\,\mu\text{m}$), $\Delta E(q_{str})$ also grows more slowly for longer cells, whereas for
119 $h = 8\,\mu\text{m}$ it is on the contrary a single function of Φ_c for both cell lengths (Fig. 2c). Importantly, when
120 normalized to its value at high Φ_c, $\Delta E(q_{str})$ was found to be for all conditions a single function of the flux of
121 bacterial mass integrated over the vortex size $\Phi_c v_0 \pi/q_{str}$, where v_0 is the population-averaged swimming
122 speed of the cells (Supplementary Fig. 4d). For $\Phi_c \lesssim 0.01$, v_0 itself is on average constant at a value
123 between 10 and $25\,\mu\text{m/s}$ which depends on cell length and the degree of confinement, and also tends to
124 vary between biological replicates (Supplementary Fig. 1b, c). At $\Phi_c \gtrsim 0.01$, v_0 progressively increases, by
125 a factor of up to two, as $\Delta E(q_{str})$ grows and the collective motion developed, consistantly with previously
126 reported behaviour [2].

Dependence of chemotaxis on cell density

128 The chemotactic response of the cells to the MeAsp gradient was first quantified using their chemotactic
129 drift velocity v_{ch}, i.e. the population-averaged speed of displacement up the gradient, measured as detailed
130 in Methods following Colin *et al.* [49]. The gradient of MeAsp concentration (from 0 to 200 μM in 2 mm)
131 was chosen to maximize v_{ch} at low cell density [49]. For all combinations of cell length L and channel
132 height h, we observed that the chemotactic drift v_{ch} first tends to increase when the cell volume fraction Φ_c
133 increases in the range $5\,10^{-4} - 0.01$. It then strongly decreases above a cell volume fraction Φ_c that depends
134 on L and h, corresponding to the one above which collective behaviour is observed (Fig. 3a). Consistantly,
135 the drift decreases as function of $\Delta E(q_{str})$, albeit differently for each L and h (Supplementary Fig. 5).
136 Swirling collective motion thus clearly impairs the ability of the cells to perform chemotaxis.

137 Since the chemotactic drift depends both on the cell swimming speed and on their ability to bias their
138 direction of motion towards the gradient – the chemotactic efficiency, we aimed to separate these two
139 contributions by normalizing v_{ch} to the swimming speed v_0. For non-interacting cells in 3D in a chemical
140 gradient, they are expected to be related by [51–53]:

$$v_{ch} = G v_0^2 \tau\left(\tau_m, \tau_T, \tau_R\right) \nabla f(c), \tag{2}$$

4

141 where G is the total gain of the chemotaxis system, $f(c)$ is the part of the chemoreceptor free energy
142 difference due to the binding of chemical ligand, present at concentration c and τ is the typical time during
143 which the bacterium is able to measure a change of $f(c)$ in a given direction. The latter depends on the
144 memory time scale τ_{m} as well as on two reorientation times. The first is due to Brownian rotational diffusion
145 during the runs, $\tau_{\mathrm{R}} = 1/D_{\mathrm{r}}$, with D_{r} the rotational diffusion constant of isolated cells. The other is due to
146 tumbling, $\tau_{\mathrm{T}} = \tau_0/(1 - \exp(-D_T\tau_{\mathrm{T}}))$, with τ_0 the steady state tumbling rate and $D_T\tau_{\mathrm{T}}$ the mean squared
147 angular change during tumbles. It is expected from previous studies [51, 52, 54] that (Supplementary Note
148 2):

$$\tau = \frac{\tau_{\mathrm{R}}}{\tau_{\mathrm{R}} + \tau_{\mathrm{T}}} \; \frac{\tau_{\mathrm{T}}}{1 + \tau_{\mathrm{T}}/\tau_{\mathrm{R}} + \tau_{\mathrm{T}}/\tau_{\mathrm{m}}} \; . \tag{3}$$

149

150 In absence of interactions, according to Eq. 2, the chemotactic coefficient v_{ch}/v_0^2 depends only on
151 internal – fixed – parameters of the chemotaxis pathway and on the fixed concentration profile. This
152 quantity was therefore chosen to quantify chemotactic efficiency at all densities, although at high densities
153 cell behaviour might deviate from Eq. 2. We observed that the chemotactic coefficient v_{ch}/v_0^2, like the
154 chemotactic drift, tends to increase with volume fraction, peaks at a condition–dependent Φ_{c} around
155 0.01, before decreasing sharply – by a factor of up to 100 – as the collective motion develops (Fig. 3b).
156 We therefore concluded that both the intermediate maximum of v_{ch} and its subsequent reduction by the
157 collective motion arise from cell-density effect on the chemotactic efficiency, and that the moderate increase
158 in swimming speed at high cell density cannot compensate for the much stronger density dependence of
159 the chemotactic coefficient.
160 Chemotaxis was also found to be affected by cell length and channel height. Even at low cell volume
161 fraction, if cells are longer or in a higher channel, they have a higher chemotactic coefficient v_{ch}/v_0^2 (Fig.
162 3b). Cell elongation is indeed expected to result in increased chemotactic coefficient in steady gradients [55],
163 because of the lower Brownian rotational diffusion of longer cells [51] and their expected reduced tumbling
164 angle [42, 56]. To directly compare the pure effect of cell density under various L and h, chemotactic
165 coefficients were normalized to the average value at low volume fractions ($\Phi_{\mathrm{c}} < 0.0015$) in each condition
166 (Fig. 3c). Even this normalized chemotactic coefficient is significantly higher for longer cells at $\Phi_{\mathrm{c}} > 0.01$
167 under moderate confinement ($h = 50$ and $30\,\mu$m, Fig. 3b). It is however a single function of Φ_{c}, irrespective
168 of cell length, for $h = 8\,\mu$m (Fig. 3c).
169 The behaviour of the chemotactic coefficient is thus reminiscent of the one of $E(q_{\mathrm{str}})$. Indeed, the
170 normalized chemotactic coefficient was found to be a single function of the amplitude of the collective
171 motion $\Delta E(q_{\mathrm{str}})$, irrespective of the cell length and channel height (Fig. 3d), decreasing exponentially as a
172 function of $\Delta E(q_{\mathrm{str}})$ from its low density value. The amplitude of the collective motion therefore appears
173 to determine the reduction of the ability to follow gradients, irrespective of vortex size π/q_{str}, for $\Phi_{\mathrm{c}} \gtrsim 0.01$,
174 in all conditions.

Collective reorientations impair chemotaxis

176 As the indirect effect of gradient distortion by the swimming bacteria could be ruled out (Fig. 1), we
177 hypothesized that the observed reduction of chemotaxis at high density is due to the forced reorienta-
178 tions resulting from the physical interactions, which would interfere with the sensing mechanism based on
179 temporal comparisons: As the cell is swimming, it monitors the change in chemoattractant concentration
180 within a few seconds, to decide whether to tumble. If during this time the direction in which the cell swims
181 has changed significantly, the decision becomes less relevant, thus making the biochemically hard-wired
182 bacterial chemotaxis strategy inefficient. In this hypothesis, collective reorientations would then act anal-

5

183 ogous to an enhancement of rotational diffusion, where the time scale of sensing τ would decrease because
184 D_r effectively increases [52, 53, 57], reducing the chemotactic coefficient accordingly (Eq. 2 and 3).

185 To test whether collective reorientations may indeed reduce chemotactic drift, we performed numerical
186 simulations of a population of self-propelled chemotactic rods of variable aspect ratio L in a viscous medium,
187 with the cell motion being confined to two dimensions. The cells interact sterically upon contact as well
188 as hydrodynamically (Fig. 4a), being transported and reoriented by the flow generated by the other cells,
189 which were approximated as pusher force dipoles in Hele-Shaw geometry [8, 58]. The strength and reach
190 of the hydrodynamic interaction is channel-height dependent in this approximation because of viscous
191 friction on the walls (Methods and Supplementary Fig. 6). Rods reorient rotationally when tumbling, with
192 the tumbling probability being determined according to the concentration of chemoattractant experienced
193 by the rod, using a model of the chemotaxis system of *E. coli* [59]. They also are subject to rotational
194 Brownian motion, with the rotational diffusion coefficient D_r being smaller for longer cells [55].

195 When the cell area fraction increases in the simulations, the rods form increasingly large swirling packs
196 of cells, similarly to previous reports, whether hydrodynamic interactions are present [8, 14, 20, 58] (full
197 simulations, Fig. 4b) or not [23, 24] (steric-only simulations, Supplementary Fig. 7). However, qualitatively
198 better agreement with experiments is achieved when hydrodynamic interactions are taken into account,
199 suggesting that they are the primary contributor to the emergence of the collective motion in this case.
200 Notably, when hydrodynamics is accounted for, the flow structure factor $E(q)$ peaks at a q_{str} which depends
201 only on channel height and not on cell density or cell length, in agreement with experiments (Fig. 4c),
202 although the simulated vortex size is smaller than the experimental one. In contrast, when only steric
203 interactions are simulated, q_{str} clearly depends on cell length (Supplementary Fig. 7d). The dependences
204 of simulated $E(q_{str})$ on channel height, cell length and cell density in the full simulations are similar to the
205 experiments (Fig. 4d). Similarly, the swimming speed v_0 increases in the full simulations, although to a
206 lesser extent than in the experiments, whereas it decreases in the steric-only case (Supplementary Fig. 8),
207 suggesting that this increase is due to hydrodynamic entrainment and further confirming the importance
208 of hydrodynamic interactions in the emergence of the collective motion.

209 In the full simulations, the chemotactic coefficient v_{ch}/v_0^2, plotted as a function of cell body area
210 fraction, decreases at the cell densities where the collective motion develops (Fig. 4e). However, contrary
211 to the experiments, no increase in chemotactic coefficient is observed at intermediate cell area fractions.
212 Nevertheless, v_{ch}/v_0^2 does scale with $E(q_{str})$, as in the experiments, although with a sharper decrease (Fig.
213 4f). In the steric-only simulations, v_{ch}/v_0^2 instead peaks as a function of cell area fraction at high densities
214 but it is not a single function of $E(q_{str})$ (Supplementary Fig. 7e).

215 Finally, we took advantage of having access to all single cell trajectories in the simulations to gain more
216 insight into the mechanism of chemotactic drift reduction. The time autocorrelation of the individual cell
217 velocity $\mathbf{v}_i$, $C_v(t) = \langle \mathbf{v}_i(t + t_0) \cdot \mathbf{v}_i(t_0) \rangle_{i,t_0} / \langle \mathbf{v}_i^2(t_0) \rangle_{i,t_0}$, shows a faster decorrelation as cell density increases
218 for all values of h and L, because of the collective reorientations (Fig. 4g). We used the decorrelation time,
219 defined as $C_v(\tau_{dec}) = 0.5$, as a measure of directional persistence (Supplementary Fig. 9a). In absence of
220 all physical interactions, the decorrelation time depends on the Brownian and tumbling reorientation times
221 as $1/\tau_{dec} = 1/\tau_R + 1/\tau_T$, and combining Eq. 2 and 3, the chemotactic coefficient can be written as:

$$\langle v_{ch}/v_0^2 \rangle = \frac{\tau_{dec}^2/\tau_T}{1 + \tau_{dec}/\tau_m} G \nabla f(c) \,. \tag{4}$$

222 At higher cell densities, τ_{dec} also includes collective reorientations, $1/\tau_{dec} = 1/\tau_R^{eff} + 1/\tau_T$, with
223 $1/\tau_R^{eff} = 1/\tau_R + 1/\tau_C$ an effective rotational diffusion rate including Brownian (τ_R) and collective (τ_C)
224 reorientation times. Despite this additional contribution of collective motion, the dependence of the sim-
225 ulated chemotactic coefficient as a function of τ_{dec} is found to follow Eq. 4 very well at all densities, with

6

226 the computed – and not fitted – coefficient values given in Supplementary Table 2, for all conditions in
227 the full simulations (Fig. 4h). The effect of simulated collective motion can therefore be interpreted as
228 an active enhancement of rotational diffusion, which decreases $\tau_{\mathrm{R}}^{\mathrm{eff}}$, hence τ_{dec} and the drift. In contrast,
229 the chemotactic coefficient does not match well the dependence on the reorientation time predicted by Eq.
230 4 when only steric interactions are taken into account (Supplementary Note 3 and Supplementary Fig.
231 6**h**). Notably, the reorientations coming from physical cell-cell interactions do not necessarily respect the
232 detailed balance of cell orientation fluxes, as Brownian rotational diffusion does, which may explain the
233 deviations from Eq. 4 that we observed even when the hydrodynamic interactions are taken into account
234 (Supplementary Note 4 and Supplementary Figs. 9 and 10).

Discussion

236 Although the principles of bacterial chemotactic sensing are fairly well understood for a single cell [29, 31],
237 little was known about the effects of physical interactions between cells on chemotaxis, despite their frequent
238 occurrence during self-concentration processes [38–43] and high-density collective motility [4, 5, 10]. While
239 the physical properties of the collective motion, e.g. in a swarming colony, are largely unaffected by activity
240 of the chemotaxis pathway [58, 60, 61], the reverse is not necessarily true. Here, we thus used suspensions
241 of *E. coli* in a controlled environment as a model system to investigate the effect of collective motion,
242 emerging when cell density increases, on chemotactic sensing.

243 We observed that the size of bacterial flow structures in fully developed collective motion is set by
244 the smallest system size, the channel height, independently of cell length and volume fraction, and that
245 an increasing amount of the kinetic energy of the system gets poured into this flow structure as the
246 cell density increases. This property strongly suggests that hydrodynamics plays the primary role in the
247 emergence of the collective motion, since, in the Hele-Shaw geometry of our system, the channel height
248 sets the reach of the hydrodynamic interaction [8], fundamentally because of viscous friction on its top and
249 bottom walls. Previous works also predicted that the largest possible flow structure – set by system size
250 – dominates in hydrodynamics-based collective motion [15, 62]. Also consistent with previous simulations
251 of such motion [63] is the observed reduction of the total kinetic energy at fixed Φ_{c} but under increased
252 confinement. Interestingly, similar flow properties are observed for the hydrodynamics-based collective
253 flows during sedimentation of dense suspensions of passive particles [64, 65]. Consistantly, our numerical
254 simulations show that considering hydrodynamic interactions is key to reproduce the main experimental
255 features, including the dependence of the vortex size on channel height, and its independence of cell
256 length. Although the simulated vortex size is smaller than in the experiments, such shifts were previously
257 observed on other quantities for this type of model [58]. Notably, besides the channel height, hydrodynamic
258 interactions also set another characteristic length in our system, the hydrodynamic dipole length. This
259 might explain the apparent saturation of the vortex size at about $20\,\mu\mathrm{m}$ in the experiments, when the
260 channel height approaches the estimated dipole length ($\sim 6\,\mu\mathrm{m}$).

261 Physical interactions between cells at high densities result in a strong reduction and ultimately in the
262 abolishment of the specific ability of *E. coli* to track chemical gradients, and thus of the chemotactic drift,
263 despite the moderate increase in swimming speed due to collective entrainment. The collective motion is
264 the driver of this decrease, with its amplitude $E(q_{\mathrm{str}})$ being the sole determinant of reduced chemotactic
265 efficiency. Collective motion acts directly on the mechanism of gradient-sensing since the gradient itself
266 is little affected. Our analysis based on agent-based simulations suggests that this reduction is induced
267 by an increased reorientation rate of cell bodies due to the collective motion, whether it emerges from
268 steric or hydrodynamic interactions, which in this sense acted similarly to an active rotational diffusion.

Importantly, we conclude that Eq. 2 derived for non-interacting swimmers can describe the chemotactic drift well at all densities, provided that the time scale of rotational diffusion is set to account not only for Brownian but also for interaction-induced reorientations. A similar reduction of chemotaxis by forced cell reorientations could be expected in other contexts, such as cells swimming in circles near surfaces [66] or during migration through a porous medium where cells collide with obstacles [67, 68].

In contrast to the inhibition at high densities, the chemotactic drift is enhanced between low and intermediate densities. Although the nature of this increase remains to be elucidated, it is unlikely to result from self-attraction [38, 39] or other chemical effects, as its extent depends on the degree of confinement and on cell length. In the simulations, a similar enhancement is observed when only steric interactions are considered – but not with the full model including hydrodynamic interactions, although it is not clear whether the nature of the transient enhancement in those simulations is the same as in the experiments. This discrepancy, along with the other quantitative differences between experiments and simulations, could potentially be explained by a number of factors our hydrodynamic simulations do not account for, such as collisions with the top and bottom channel walls and other physical effects neglected by two-dimensional confinement, flagellar entanglements and fluid flows affecting the flagellar bundles stability [69], as well as the point force approximation.

The observed regulation of chemotactic behaviour through physical interactions among motile cells has several important consequences for bacterial high-density behaviours. First, it provides a physical mechanism that might regulate chemotactic accumulation of bacteria near sources of chemoattractants (e.g., nutrients), because gradually increasing cell density [70] would initially promote and subsequently limit the process. Indeed, this effect could explain why the density of cells entering a capillary filled with chemoattractant saturates as a function of the cell density in the suspension [71]. The density for which the chemotactic drift is maximal, $\Phi_c \simeq 0.01$, which should play a cut-off role, is indeed the typical maximal cell density reached within travelling chemotactic bands which form through a self-generated gradient [42, 43]. Thus, the hitherto neglected effects of physical interactions should be taken into account when describing these phenomena, in conditions for which the density gets high. Second, the observed strong reduction in chemotactic drift at cell densities typical of swarming ($\Phi_c \sim 0.30$) [5] suggests that, without specific counteracting mechanisms, chemotactic navigation of bacteria swimming within a swarm is nearly impossible, consistent with recent indications that the swarm expansion rate is set by the cell growth rate rather than motility [8]. Interestingly, we observed that cell elongation, one of the major hallmarks of swarming bacteria [4], indeed improved chemotaxis at high Φ_c under moderate confinement. However, it appeared to have little effect under stronger confinement expected in the swarm. Bacterial swarming was already known to be unaffected by the lack of functional chemotactic sensing [60, 61]. Although more prominent steric interactions within a swarming colony [7, 8] might potentially improve tracking of gradients at high density, as could other differences in swimming behaviour [72, 73], or additional cohesive interactions [44] caused by cell differentiation in a swarm, our results suggest that the emergence of swirling collective motion fundamentally undermines the chemotactic behaviour.

Methods

Strains and cell culture

Escherichia coli strain W3110 (RpoS+), *flu+* or Δflu [38], were grown at 34 ^{o}C in Tryptone Broth (TB) from a 100-fold dilution of overnight culture to an optical density at 600 nm $OD_{600} = 0.7$. Where applicable, the culture was supplemented with 0.01 % cephalexin at one division time (1 h) before harvesting the cells. Cells were washed thrice and resuspended in motility buffer (10 mM KPO$_4$, 0.1 mM EDTA, 67 mM NaCl,

312 pH 7.0) supplemented with 55 mM glucose as energy source, cooled to 4 ^{o}C for 20 min to reduce metabolic
313 activity and then concentrated by centrifugation ($1.5 \, 10^3$ g, 7 min) to a final cell density of $\Phi_c \sim 0.20$
314 ($OD_{600} \sim 100$). Series of dilutions were then performed in motility buffer, so that the amount of glucose
315 per cell remains constant for all cell densities (~ 0.5 mM/OD_{600}).

Microfabrication

317 Molds were fabricated using standard photolithography and microfabrication techniques. The SU8 pho-
318 toresist (Microchem™) was spincoated on a silicon wafer for 90 s, covered with a positive mask of the
319 device, produced using AutoCAD and printed by JD Photo Data (UK), and exposed to UV light, baked
320 and developed according to manufacturer instructions. SU8 grade and spincoat speeds are indicated in
321 Supplementary Table 1. Poly-di-methylsiloxane (PDMS), in a 1:10 crosslinker to base ratio, was poured on
322 the cast, degazed, baked overnight at 70° C, peeled off, cut to shape and covalently bound on isopropanol-
323 rinsed microscopy glass slides after oxygen plasma treatment. PDMS to glass covalent bounds were allowed
324 to form for 15 minutes at room temperature and the devices were then filled with sterile DI water for short
325 term storage (few hours), in order to retain their hydrophilic properties.

Chemotaxis assay

327 The assay was described in detail previously [49]. In the microfluidic device (Fig. 1a), the two reservoirs
328 were filled with cell suspensions of the same volume fraction supplemented with either no or 200 μM α-
329 methyl-D,L-aspartic acid (MeAsp), and then sealed to avoid residual flows. The MeAsp gradient formed in
330 the 2 mm long, 1 mm wide, channel connecting them. Bacterial motion in the middle of the channel was
331 recorded thrice, at one hour interval, at mid-height, in phase contrast microscopy at 10$\times$ magnification,
332 using a Mikrotron 4CXP camera (1 px = 1.4 μm, field of view $A_0 = 512 \times 512$ px^2, 1 ms exposure) running
333 at 100 frames/s (fps).

Gradient calibration

335 For gradient calibration experiments, the suspensions - at various cell densities - in the second reservoir
336 were supplemented with 100 μM fluorescein as well as attractant. The gradient was measured in wide-field
337 fluorescence microscopy (excitation filter 470/40, emission 525/50) at 10$\times$ magnification. Images were
338 recorded using an Andor Zyla 4.2 sCMOS camera in the middle of the channel and in the attractant
339 reservoir, the former being divided by the latter to correct for inhomogeneous illumination.

Motility measurements by Fourier image analysis

341 Cell motility was quantified by analysing the movies with three different algorithms. The first is differential
342 dynamic microscopy (DDM), a now well established technique [46, 47], computing differential image corre-
343 lation functions (DICF), which were fitted to extract the average swimming speed of the population of cells
344 v_0 and the fraction of swimming cells α, as well as the local cell density (see below). The shortcomings due
345 to the breakdown of two assumptions of Wilson *et al.* [46] – even distributions of swimming directions and
346 round cell images – were accounted for via calibrations (see below). Second, phase differential microscopy
347 (ΦDM) [49] determined the population averaged drift velocity of the population of cells $v_d = \langle v_x(i,t) \rangle_{i,t}$,
348 with positive x being the up-gradient direction, i cell index and t frame number. The chemotactic velocity,
349 corrected for the fraction of non swimming cells, is then $v_{ch} = v_d/\alpha$. Lastly, maps of the local velocity
350 field were obtained by using a local ΦDM algorithm described in detail below. This image velocimetry

9

351 technique estimated the velocity of a group of few cells located within a region $5\,\mu$m in diameter around a
352 position $\mathbf{r} = (x, y)$. The local velocity field $\mathbf{v}(\mathbf{r}, t)$ was thus calculated for each time point t, and its spatial
353 Fourier transform, $\tilde{\mathbf{v}}(\mathbf{q}, t) = \iint d\mathbf{r}\,\mathbf{v}(\mathbf{r}, t)\exp\left(-i\mathbf{q}.\mathbf{r}\right)$, then led to the flow structure factor via Eq. 1.

Local image velocimetry algorithm

355 The image analysis algorithm is as follows, with parameter values as chosen for our analysis: In a movie
356 of $T = 10^4$ frames of size $A_0 = L_0 \times L_0$ pixels ($L_0 = 512$), the local velocities are computed at points
357 situated on a square lattice spaced by a distance $da = 4$ px, starting from a distance $a/2$ from the edges of
358 the frame ($a = 32$ px). For this, submovies of size $a \times a$ are considered, each centered on one of the points
359 (represented by the index k in the following) . The spatial discrete Fourier transform of the blurred time
360 frame t in the submovie k is computed as:

$$I_k^{bl}(\mathbf{q}, t) = \iint \mathrm{d}r I_k(\mathbf{r}, t)\exp\left(-\mathbf{r}^2/l^2\right)\exp\left(-i\mathbf{q}\mathbf{r}\right)\,, \tag{5}$$

361 where $r = 0$ in the center of the submovie and $l = 3$ px is a filtering range. The size of the group of cells, for
362 which the instantaneous velocity is computed, can thus be tuned independently of the Fourier transform
363 parameters. Changes in pixel intensities at a distance farther than l will not contribute to the evaluation
364 of the velocity at the point considered.
365 In the fashion of ΦDM [49], the phase $\delta\phi_k(\mathbf{q}, t)$ of the complex correlator $I_k^{bl}(\mathbf{q}, t+1)I_k^{bl}(\mathbf{q}, t)^*$ is
366 computed and summed to get $\phi_k(\mathbf{q}, t) = \sum_{t'=0}^{t-1} \delta\phi_k(\mathbf{q}, t')$. This phase is fitted as a function of $\mathbf{q}$ to get
367 the cummulated displacement $\mathbf{r}_k(t)$, $\phi_k(\mathbf{q}, t) = \mathbf{q} \cdot \mathbf{r}_k(t)$ [49]. The local instantaneous velocity $\mathbf{v}_k(t)$ is then
368 computed by fitting:

$$\mathbf{r}_k(t') = \mathbf{r}_k(t) + \mathbf{v}_k(t)(t' - t) \tag{6}$$

369 on a range of $\tau = 20$ frames centered on t. Note that this method for measuring local displacements is equiv-
370 alent to particle image velocimetry (PIV), since the phase of the correlation in Fourier space corresponds
371 to the peak of the image cross-correlation in real space used in PIV to measure such displacement.

In situ measurement and calibration of cell body volume fraction

373 Chemotaxis microfluidic chips without a chemoattractant gradient were filled with suspensions of defined
374 cell concentration, measured by OD_{600}. The differential image correlation functions (DCIF) $g(q, \tau) =$
375 $\langle |I(\mathbf{q}, t+\tau) - I(\mathbf{q}, t)|^2\rangle_{t, |\mathbf{q}|=q}$ were computed from DDM and fitted according to

$$g(q, \tau) = a_0(q) + a_1(q)(1 - f(q, \tau))\,, \tag{7}$$

376 where $f(q, \tau)$ is the intermediate scattering function yielding the cells average swimming speed and fraction
377 of swimmers [46, 47]. The amplitude $a_1 \simeq g(q, +\infty) = 2\langle |I(\mathbf{q}, t)|^2\rangle_{t, |\mathbf{q}|=q}$ is expected to scale as $a_1(q) \sim$
378 $f(N_{\text{part}})\langle I\rangle^2 F(q)S(q)$, where N_{part} is the number of bacteria in the field of view, $S(q)$ is the structure
379 factor of the bacterial fluid and $F(q)$ is a form factor describing the shape of the bacteria. As can be
380 seen in Supplementary Fig. 2**a**, $a_1(q)/\langle I\rangle^2$ has a single maximum for each OD_{600}. This maximum was
381 found to obey the equation $a_1^{\max}/\langle I\rangle^2 = 1.25\,m\,OD_{600}/(1 + m\,OD_{600})$ (Supplementary Fig. 2**b**), where m
382 is a constant depending on the length of the bacteria and the height of the channel, for channel heights
383 $h = 50\,\mu$m and $h = 30\,\mu$m. In the channel height $h = 8\,\mu$m, the data were more scattered due to
384 the difficulty of obtaining a truly homogeneous suspension even in absence of gradient, and the equation
385 $a_1^{\max}/\langle I\rangle^2 = d_0\,m\,OD_{600}/(1 + m\,OD_{600})$, with d_0 also depending on cell length, was found to better fit

10

386 the data (Supplementary Fig. 2**c**). In all experiments, we then used $a_1^{\max}/\langle I \rangle^2$ obtained from the DDM
387 measurement to evaluate the local OD_{600} via the appropriate equation.

388   The correspondance between optical density and cell body volume fraction was determined by counting
389 cells in suspensions of known OD_{600} flowing at 17.5 μL/min in a flow cytometer (BD Fortessa), which led
390 to a size-dependent correspondance between cell number density (n_c) and OD_{600}. The average length L
391 of the cells was evaluated by segmenting and fitting as ellipses phase contrast microscopy images of the
392 cells (magnification $\times 40$, NA 0.95) using ImageJ (Rasband, W.S., ImageJ, U. S. National Institutes of
393 Health, Bethesda, Maryland, USA, http://imagej.nih.gov/ij/, 1997-2016.). The cell body volume fraction
394 was then $\Phi_c = \pi r^2 L n_c$, where $r = 0.5 \, \mu$m is the radius of an *E. coli* cell. The volume fraction was found to
395 be proportional to optical density for both cell sizes, $\Phi_c = (1.78 \pm 0.03) \, 10^{-3} \, OD_{600}$ (Supplementary Fig.
396 2**d**), yielding the local Φ_c for all experiments.

Calibrations of the swimming speed measurement

398 **Confinement effect compensation** –   Classical fits of the intermediate scattering function [46] assume
399 that the cells are swimming in 3D with equal probability in all directions. Biased swimming directions in
400 the plane of the field of view were also shown to not affect the measurement as long as the swimming speed
401 of the cells is the same in all directions [49] (in other words, if chemotaxis, but not chemokinesis, biases
402 swimming). If the distribution of swimming directions is however biased in the direction perpendicular
403 to the field of view (z), the measured velocity *will* be systematically biased. This was notably the case
404 when the suspension gets confined towards two dimensions, in the $h = 30$ and $8 \, \mu$m channels. Analytical
405 predictions exist for the DICF both for the 3D and 2D cases, but intermediate situations are more complex;
406 The 3D analytical expression was thus used to extract the velocity and corrected as follows.

407   Since cells are partially confined in the z direction, we expect that the swimming speed v_0 measured
408 using the formula, valid for cells swimming isotropically in three dimensions [46]:

$$f(q,\tau) = e^{-Dq^2\tau} \left(1 - \alpha + \alpha \left(\frac{Z+1}{Zqv_0\tau} \right) \frac{\sin\left(Z^{-1}\tan^{-1}\lambda \right)}{(1+\lambda^2)^{Z/2}} \right), \tag{8}$$

409 with $\sigma_v = v_0/\sqrt{Z+1}$ and $\lambda = qv_0\tau/(Z+1)$, will be systematically biased compared to the real velocity. To
410 evaluate this bias, the following experiment was conducted. The PDMS chips with 50 μm and 30 μm height
411 were bound by plasma treatment facing each other and to a glass slide (Supplementary Fig. 11**a**). Cell
412 suspensions at $OD_{600} \simeq 1$ were flown in the chamber – without a gradient created – and let to equilibrate
413 for one hour. The motion of the bacteria was recorded successively in the two channels of different heights
414 and the effective swimming speed v_0 was extracted using equations 7 and 8 for both channels. The ratio
415 $v_0(30)/v_0(50)$ was found to be 1.075 ± 0.01 (SD – $N = 10$ repeats). The ratio being higher than 1 was
416 expected since confinement makes the horizontal runs more probable and therefore increases the apparent
417 3D velocity. The same game played on the $h = 8 \, \mu$m channel lead to a ratio $v_0(8)/v_0(50) = 1.14 \pm 0.02$
418 (SD – $N = 5$ repeats). All effective velocities obtained by 3D fitting in both devices of lower heights were
419 divided by the corresponding factor to deduce the real swimming speed.

420 **Effect of cell length** –   The formula 7 is valid only in the case of bacteria with isotropic shapes or for
421 which the orientation of the anisotropic shape is uncorrelated with the direction of motion. This is a good
422 approximation in the case of $2 \, \mu$m long cells observed in phase contrast at $10\times$ magnification, but not
423 anymore for $4 \, \mu$m long cells in these conditions. For anisotropic objects like rods, equation 7 becomes, in

the non interacting case:

$$g(q,\tau) = a_0(q) + \langle I^2 \rangle S(q) \int_0^{2\pi} \langle F(q,\theta) f(q,\theta,v\tau) \rangle \mathrm{d}\theta \tag{9}$$

were θ measures the orientation of the rods. Only when q becomes smaller than $1/a$, a being the largest size of the objects, does $F(q,\theta) \to 1$, and $g(q,\tau)$ can be fitted as in Wilson *et al.*[46] (Eqs. 8 and 7) irrespective of the shape of the particles. The outcome $v_0(q)$ of the fit of the DICF is plotted for randomly chosen experiments with non-treated and elongated cells in Supplementary Fig. 11**b**. For elongated cells, above $q = 0.9$ px^{-1}, the fitted v_0 decreased because of the anisotropy. We therefore used the values of v_0 in the range $q = 0.4 - 0.9$ px^{-1} to evaluate the swimming speed in the case of elongated cells, whereas $q = 0.4 - 2.0$ px^{-1} was used for the normal cells.

Simulations

We performed agent-based simulations of the rod-like – length L, width e – chemotactic particles in two dimensions in a $256 \times 256 \,\mu\mathrm{m}^2$ box with periodic boundary conditions. The particles are self-propelled in an overdamped fluid at constant propulsion force and interacted by exerting forces and torques on each other in the form of a Hertzian repulsion $\mathbf{F}_{ij}^{\mathrm{el}}$, a friction $\mathbf{F}_{ij}^{\mathrm{fr}}$ and far-field hydrodynamic interactions, which we accounted for following Jeckel *et al.* [8]. We write $\mathbf{F}_{ij}^{\mathrm{tot}} = \mathbf{F}_{ij}^{\mathrm{el}} + \mathbf{F}_{ij}^{\mathrm{fr}}$ the sum of the elastic repulsion and friction generated upon contact by particle j on i:

$$\mathbf{F}_{ij}^{\mathrm{el}} = K_{\mathrm{el}}\, \delta_{i,j}^{3/2}\, \mathbf{u}_{ij}\,, \tag{10}$$

$$\mathbf{F}_{ij}^{\mathrm{fr}} = -K_{\mathrm{fr}}(\mathbf{v}_i - \mathbf{v}_j) \cdot \mathbf{v}_{ij}\, \mathbf{v}_{ij}\,, \tag{11}$$

with $\mathbf{u}_{ij}$ and $\mathbf{v}_{ij}$ the normalized orthogonal vectors defined in the inset of Fig. 4**a**, $\delta_{i,j}$ the inter-penetration depth between particle i and j. The free running velocity of particle i is $\mathbf{v}_i = v_i \mathbf{n}_i$, with a norm v_i chosen randomly in a Gaussian distribution of mean v_0 and variance dv_0 and direction $\mathbf{n}_i = (\cos(\theta_i), \sin(\theta_i))$. Note that $\mathbf{F}^{\mathrm{fr}}$, which was not included in previous studies [22–24], could be interpreted as effectively resulting from short-range cell-cell interactions including viscous shear in the thin liquid film between two cells, complex flagellar entanglement, and solid friction. The particles can be in two states, either running ($\Theta_i = 1$) or tumbling ($\Theta_i = 0$). During tumbles, self-propulsion is switched off and a random torque made the particle turn, with an average magnitude chosen to match literature reported turning angle distributions [74]. The equations of motion for their position $\mathbf{r}_i$ and orientation θ_i are therefore:

$$\frac{d\mathbf{r}_i}{dt} = \Theta_i\, v_i \mathbf{n}_i + \Sigma_j \frac{\mathbf{w}_j(\mathbf{r}_i) + \mathbf{w}_j(\mathbf{r}_i - L_{\mathrm{dip}}\mathbf{n}_i)}{2} + (\gamma_\perp^{-1}\mathbf{I} + (\gamma_\parallel^{-1} - \gamma_\perp^{-1})\mathbf{n}_i\mathbf{n}_i)\Sigma_j \mathbf{F}_{ij}^{\mathrm{tot}} \tag{12}$$

$$\frac{d\theta_i}{dt} = \sqrt{D_{\mathrm{r}}}\eta_{\mathrm{r}}(t) + \sqrt{D_{\mathrm{T}}}\eta_{\mathrm{T}}(t)\,(1 - \Theta_i) + \mathbf{n}_i \wedge \Sigma_j \left(\frac{\mathbf{w}_j(\mathbf{r}_i) - \mathbf{w}_j(\mathbf{r}_i - L_{\mathrm{dip}}\mathbf{n}_i)}{L_{\mathrm{dip}}} + \gamma_r^{-1} l_{i,j}\mathbf{F}_{ij}^{\mathrm{tot}} \right)\,. \tag{13}$$

The translational friction coefficients read $\gamma_\parallel = 2\pi\eta L/\ln(L/e)$ and $\gamma_\perp = 2\gamma_\parallel$, and $\gamma_r = \gamma_\parallel L^2/6$ is the rotational friction coefficient. The distance between the center of mass of the particle and the contact point with particle j is $l_{i,j}$. Rotational Brownian motion is modelled using the rotational diffusion coefficient D_{r} and the normal Gaussian noise $\eta_{\mathrm{r}}(t)$, and reorientation during tumbles using corresponding D_{T} and $\eta_{\mathrm{T}}(t)$.

When hydrodynamic interactions are included, $\mathbf{w}_j(\mathbf{r})$ is the flow generated by particle j at point $\mathbf{r}$. The particles thus react to external flows as a dumbell. As a source of flow, they are modeled as a dipole

of point forces of pusher symmetry (Fig. **4a**). The point of application of the resistive force coincides with the center of the rod, the one of the propulsive force being situated $L_{\text{dip}} = L/2 + L_{\text{flag}}/2$ behind the latter in the direction of the rod. Following Jeckel *et al.* [8], we used a quasi-2D approximation to compute the flow generated by the 2D point force $\mathbf{F} = \gamma_{\parallel} v_j \mathbf{n}_j$. The fluid velocity $\mathbf{u}$ is assumed to take a Poiseuille profile in the z-direction, its average (x,y)-component $\mathbf{U} = 1/h \int_0^h \mathbf{u}(x, y, z) dz$ thus obeying an effective 2D Hele-Shaw equation:

$$\nabla \cdot \mathbf{U} = 0 \tag{14}$$

$$\nabla P - \eta(\nabla^2 \mathbf{U} - \kappa \mathbf{U}) = \frac{\mathbf{F}}{h} \delta^{(2)}(\mathbf{r}) \tag{15}$$

where P is the pressure, $\nabla = (\partial_x, \partial_y)$ and $\kappa = 12/h^2$, the origin being taken at the point of application of $\mathbf{F}$. This equation was solved in Jeckel *et al.* [8]:

$$\mathbf{U} = \mathbf{G} \cdot \mathbf{F} \tag{16}$$

with the symmetric matrix:

$$\mathbf{G} = \frac{1}{\pi \eta h \, \kappa |r|^2} \left[c_1(\sqrt{\kappa}|r|)\mathbf{I} + c_2(\sqrt{\kappa}|r|)\hat{\mathbf{r}}\hat{\mathbf{r}} \right] \tag{17}$$

where $\hat{\mathbf{r}} = \mathbf{r}/|r|$ and the factors:

$$c_1(z) = z^2 \left[K_0(z) + K_2(z) \right]/2 - 1 \tag{18}$$

$$c_2(z) = 2 - z^2 K_2(z) \tag{19}$$

where K_n are modified Bessel functions of the second kind. The flow generated by particle j at a position $\mathbf{r}$ from the center of the rod is then:

$$\mathbf{w}_j(\mathbf{r}) = \mathbf{U}(\mathbf{F}_j, \mathbf{r}) + \mathbf{U}(-\mathbf{F}_j, \mathbf{r} + L_{\text{dip}}\mathbf{n}_j) \tag{20}$$

which we compute as such in the algorithm, because the dipole approximation do not model short range flows accurately enough for our simulations. Note that the range of the interaction is set by the height of the channel via κ. Interestingly, the term $\eta\kappa\mathbf{U}$ which introduces this scaling in Eq. 15 comes from a term of friction on the wall $(-\eta(\partial_z \mathbf{u}(h) - \partial_z \mathbf{u}(0)))$ which appears when averaging the 3D Stockes equation over the channel height. The fluid flow is plotted for the three channel heights we used in Supplementary Fig. **6a**. When the height increases, the flow field goes from circular flow patterns to a pattern qualitatively more akin to 3D dipoles (although quantitatively different).

Finally, the state of each particle (Θ_i) was determined by an internal chemotaxis system evolving according to the ligand concentration experienced by the cells, first formulated in Vladimirov *et al.* [59], with the only difference that the instantaneous tumble probability was set directly using the concentration of phosphorylated CheY (CheY-P), disregarding the existence of multiple flagellar motors. This model is detailed in Supplementary Note 2.

The set of equations 10-13, 16-20 and Supplementary Eqs. 1-8, which governs the position and orientation of the rods, was solved by Euler integration. Parameter values [59, 75] are given in Supplementary Table S2.

Data availability

The data supporting the findings of this study, including raw images and movies, are available upon request from the corresponding authors.

Code availability

The source codes of the image analysis methods are available at https://github.com/croelmiyn/FourierImageAnalysis under MIT Licence and can be accessed and cited using https://dx.doi.org/10.5281/zenodo.3516258. The code of the simulations is available at https://github.com/croelmiyn/SimulationsChemotaxis under MIT Licence. The source code can be accessed and cited using https://dx.doi.org/10.5281/zenodo.3516624. All codes were writen in Java v1.8.0 and implemented in the form of Plugins for ImageJ v1.49.

Acknowledgements

Author contributions

R.C. and V.S. designed the research, R.C. performed and analyzed the experiments and simulations, K.D. contributed to simulations, R.C., K.D. and V.S. wrote the manuscript.

References

[1] Dombrowski, C., Cisneros, L., Chatkaew, S., Goldstein, R. E. & Kessler, J. O. Self-concentration and large-scale coherence in bacterial dynamics. *Phys. Rev. Lett.* **93**, 098103 (2004).

[2] Sokolov, A., Aranson, I. S., Kessler, J. O. & Goldstein, R. E. Concentration dependence of the collective dynamics of swimming bacteria. *Phys. Rev. Lett.* **98**, 158102 (2007).

[3] Marchetti, M. C. *et al.* Hydrodynamics of soft active matter. *Rev. Mod. Phys.* **85** (2013).

[4] Kearns, D. B. A field guide to bacterial swarming motility. *Nat. Rev. Microbiol.* **8**, 634–644 (2010).

[5] Darnton, N. C., Turner, L., Rojevsky, S. & Berg, H. C. Dynamics of bacterial swarming. *Biophys. J.* **98**, 2082–2090 (2010).

[6] Chen, C., Liu, S., Shi, X.-q., Chaté, H. & Wu, Y. Weak synchronization and large-scale collective oscillation in dense bacterial suspensions. *Nature* **542**, 210 – 214 (2017).

[7] Ilkanaiv, B., Kearns, D. B., Ariel, G. & Be'er, A. Effect of cell aspect ratio on swarming bacteria. *Phys. Rev. Lett.* **118**, 158002 (2017).

[8] Jeckel, H. *et al.* Learning the space-time phase diagram of bacterial swarm expansion. *Proc. Natl Acad. Sci. USA* **116**, 1489–1494 (2019).

[9] Stickler, D. & Hughes, G. Ability of *Proteus mirabilis* to swarm over urethral catheters. *Eur. J. Clin. Microbiol. Infect. Dis.* **18**, 206–8 (1999).

[10] Ardre, M., Henry, H., Douarche, C. & Plapp, M. An individual-based model for biofilm formation at liquid surfaces. *Phys. Biol.* **12**, 066015 (2015).

[11] Sokolov, A. & Aranson, I. S. Physical properties of collective motion in suspensions of bacteria. *Phys. Rev. Lett.* **109**, 248109 (2012).

[12] Dunkel, J. *et al.* Fluid dynamics of bacterial turbulence. *Phys. Rev. Lett.* **110**, 228102 (2013).

[13] Gachelin, J., Rousselet, A., Lindner, A. & Clement, E. Collective motion in an active suspension of *Escherichia coli* bacteria. *New J. Phys.* **16**, 025003 (2014).

[14] Lushi, E., Wioland, H. & Goldstein, R. E. Fluid flows created by swimming bacteria drive self-organization in confined suspensions. *Proc. Natl Acad. Sci. USA* **111**, 9733–9738 (2014).

[15] Saintillan, D. & Shelley, M. J. Instabilities, pattern formation, and mixing in active suspensions. *Phys. Fluids* **20**, 123304 (2008).

[16] Wolgemuth, C. W. Collective swimming and the dynamics of bacterial turbulence. *Biophys. J.* **95**, 1564–1574 (2008).

[17] Baskaran, A. & Marchetti, M. C. Statistical mechanics and hydrodynamics of bacterial suspensions. *Proc. Natl Acad. Sci. USA* **106**, 15567–15572 (2009).

[18] Decoene, A., Martin, S. & Maury, B. Microscopic modelling of active bacterial suspensions. *Math. Model. Nat. Phenom.* **6**, 98–129 (2011).

[19] Subramanian, G., Koch, D. L. & Fitzgibbon, S. R. The stability of a homogeneous suspension of chemotactic bacteria. *Phys. Fluids* **23**, 041901 (2011).

[20] Wensink, H. H. *et al.* Meso-scale turbulence in living fluids. *Proc. Natl Acad. Sci. USA* **109**, 14308–14313 (2012).

[21] Vicsek, T., Czirok, A., Ben-Jacob, E., Cohen, I. I. & Shochet, O. Novel type of phase transition in a system of self-driven particles. *Phys. Rev. Lett.* **75**, 1226–1229 (1995).

[22] Ginelli, F., Peruani, F., Bar, M. & Chate, H. Large-scale collective properties of self-propelled rods. *Phys. Rev. Lett.* **104**, 184502 (2010).

[23] Wensink, H. H. & Lowen, H. Emergent states in dense systems of active rods: from swarming to turbulence. *J. Phys. Condens. Matter* **24**, 464130 (2012).

[24] Abkenar, M., Marx, K., Auth, T. & Gompper, G. Collective behavior of penetrable self-propelled rods in two dimensions. *Phys. Rev. E* **88**, 062314 (2013).

[25] Liao, Q., Subramanian, G., DeLisa, M. P., Koch, D. L. & Wu, M. M. Pair velocity correlations among swimming *Escherichia coli* bacteria are determined by force-quadrupole hydrodynamic interactions. *Phys. Fluids* **19**, 061701 (2007).

[26] Drescher, K., Dunkel, J., Cisneros, L. H., Ganguly, S. & Goldstein, R. E. Fluid dynamics and noise in bacterial cell-cell and cell-surface scattering. *Proc. Natl Acad. Sci. USA* **108**, 10940–10945 (2011).

[27] Ezhilan, B., Shelley, M. J. & Saintillan, D. Instabilities and nonlinear dynamics of concentrated active suspensions. *Phys. Fluids* **25**, 070607 (2013).

[28] Berg, H. C. *Random Walks in Biology* (Princeton University Press, Princeton, NJ, 1983).

[29] Colin, R. & Sourjik, V. Emergent properties of bacterial chemotaxis pathway. *Curr. Opin. Microbiol.* **39**, 24–33 (2017).

[30] Sourjik, V. & Wingreen, N. S. Responding to chemical gradients: bacterial chemotaxis. *Curr. Opin. Cell Biol.* **24**, 262–268 (2012).

[31] Tu, Y. Quantitative modeling of bacterial chemotaxis: signal amplification and accurate adaptation. *Annu. Rev. Biophys.* **42**, 337–59 (2013).

[32] Larsen, S. H., Reader, R. W., Kort, E. N., Tso, W. W. & Adler, J. Change in direction of flagellar rotation is basis of chemotactic response in *Escherichia coli. Nature* **249**, 74–77 (1974).

[33] Stock, J. B., Ninfa, A. J. & Stock, A. M. Protein phosphorylation and regulation of adaptive responses in bacteria. *Microbiol. Rev.* **53**, 450–490 (1989).

[34] Goy, M. F., Springer, M. S. & Adler, J. Sensory transduction in *Escherichia coli* - role of a protein methylation reaction in sensory adaptation. *Proc. Natl Acad. Sci. USA* **74**, 4964–4968 (1977).

[35] Yi, T. M., Huang, Y., Simon, M. I. & Doyle, J. Robust perfect adaptation in bacterial chemotaxis through integral feedback control. *Proc. Natl Acad. Sci. USA* **97**, 4649–4653 (2000).

[36] Segall, J. E., Block, S. M. & Berg, H. C. Temporal comparisons in bacterial chemotaxis. *Proc. Natl Acad. Sci. USA* **83**, 8987–8991 (1986).

[37] Park, H. *et al.* Interdependence of behavioural variability and response to small stimuli in bacteria. *Nature* **468**, 819–U114 (2010).

[38] Laganenka, L., Colin, R. & Sourjik, V. Chemotaxis towards autoinducer 2 mediates autoaggregation in *Escherichia coli. Nat. Commun.* **7**, 12984 (2016).

[39] Jani, S., Seely, A. L., Peabody, V. G., Jayaraman, A. & Manson, M. D. Chemotaxis to self-generated AI-2 promotes biofilm formation in *Escherichia coli. Microbiol.* **163**, 1778–1790 (2017).

[40] Budrene, E. O. & Berg, H. C. Dynamics of formation of symmetrical patterns by chemotactic bacteria. *Nature* **376**, 49–53 (1995).

[41] Park, S. *et al.* Influence of topology on bacterial social interaction. *Proc. Natl Acad. Sci. USA* **100**, 13910–13915 (2003).

[42] Saragosti, J. *et al.* Directional persistence of chemotactic bacteria in a traveling concentration wave. *Proc. Natl Acad. Sci. USA* **108**, 16235–16240 (2011).

[43] Fu, X. *et al.* Spatial self-organization resolves conflicts between individuality and collective migration. *Nat. Commun.* **9**, 2177 (2018).

[44] Anyan, M. E. *et al.* Type IV pili interactions promote intercellular association and moderate swarming of *Pseudomonas aeruginosa. Proc. Natl Acad. Sci. USA* **111**, 18013–18018 (2014).

[45] Lushi, E., Goldstein, R. E. & Shelley, M. J. Collective chemotactic dynamics in the presence of self-generated fluid flows. *Phys. Rev. E* **86**, 040902 (2012).

16

[46] Wilson, L. G. *et al.* Differential dynamic microscopy of bacterial motility. *Phys. Rev. Lett.* **106**, 018101 (2011).

[47] Martinez, V. A. *et al.* Differential dynamic microscopy: A high-throughput method for characterizing the motility of microorganisms. *Biophys. J.* **103**, 1637–1647 (2012).

[48] Giavazzi, F. & Cerbino, R. Digital Fourier microscopy for soft matter dynamics. *J. Opt.* **16**, 083001 (2014).

[49] Colin, R., Zhang, R. & Wilson, L. G. Fast, high-throughput measurement of collective behaviour in a bacterial population. *J. Royal Soc. Interface* **11**, 0486 (2014).

[50] Kim, M. J. & Breuer, K. S. Enhanced diffusion due to motile bacteria. *Phys. Fluids* **16**, L78–L81 (2004).

[51] Dufour, Y. S., Fu, X., Hernandez-Nunez, L. & Emonet, T. Limits of feedback control in bacterial chemotaxis. *PLOS Comput. Biol.* **10**, e1003694 (2014).

[52] Celani, A., Shimizu, T. S. & Vergassola, M. Molecular and functional aspects of bacterial chemotaxis. *J. Stat. Phys.* **144**, 219–240 (2011).

[53] Si, G., Wu, T., Ouyang, Q. & Tu, Y. Pathway-based mean-field model for *Escherichia coli* chemotaxis. *Phys. Rev. Lett.* **109**, 048101 (2012).

[54] Long, J., Zucker, S. & Emonet, T. Feedback between motion and sensation provides nonlinear boost in run-and-tumble navigation. *PLOS Comput. Biol.* **13**, e1005429 (2017).

[55] Schauer, O. *et al.* Motility and chemotaxis of bacteria-driven microswimmers fabricated using antigen 43-mediated biotin display. *Sci. Rep.* **8**, 9801 (2018).

[56] Vladimirov, N., Lebiedz, D. & Sourjik, V. Predicted auxiliary navigation mechanism of peritrichously flagellated chemotactic bacteria. *PLOS Comput. Biol.* **6**, e1000717 (2010).

[57] Hu, B. & Tu, Y. Behaviors and strategies of bacterial navigation in chemical and nonchemical gradients. *PLOS Comput. Biol.* **10**, e1003672 (2014).

[58] Ariel, G. *et al.* Collective dynamics of two-dimensional swimming bacteria: Experiments and models. *Phys. Rev. E* **98**, 032415 (2018).

[59] Vladimirov, N., Lovdok, L., Lebiedz, D. & Sourjik, V. Dependence of bacterial chemotaxis on gradient shape and adaptation rate. *PLOS Comput. Biol.* **4**, e1000242 (2008).

[60] Burkart, M., Toguchi, A. & Harshey, R. M. The chemotaxis system, but not chemotaxis, is essential for swarming motility in *Escherichia coli. Proc. Natl Acad. Sci. USA* **95**, 2568–2573 (1998).

[61] Mariconda, S., Wang, Q. F. & Harshey, R. M. A mechanical role for the chemotaxis system in swarming motility. *Mol. Microbiol.* **60**, 1590–1602 (2006).

[62] Stenhammar, J., Nardini, C., Nash, R. W., Marenduzzo, D. & Morozov, A. Role of correlations in the collective behavior of microswimmer suspensions. *Phys. Rev. Lett.* **119**, 028005 (2017).

[63] Krishnamurthy, D. & Subramanian, G. Collective motion in a suspension of micro-swimmers that run-and-tumble and rotary diffuse. *J. Fluid Mech.* **781**, 422–466 (2015).

[64] Segre, P. N., Herbolzheimer, E. & Chaikin, P. M. Long-range correlations in sedimentation. *Phys. Rev. Lett.* **79**, 2574–2577 (1997).

[65] Tee, S. Y. *et al.* Nonuniversial velocity fluctuations of sedimenting particles. *Phys. Rev. Lett.* **89**, 054501 (2002).

[66] Lauga, E., DiLuzio, W. R., Whitesides, G. M. & Stone, H. A. Swimming in circles: Motion of bacteria near solid boundaries. *Biophys. J.* **90**, 400–412 (2006).

[67] Sosa-Hernandez, J. E., Santillan, M. & Santana-Solano, J. Motility of *Escherichia coli* in a quasi-two-dimensional porous medium. *Phys. Rev. E* **95**, 032404 (2017).

[68] Croze, O. A., Ferguson, G. P., Cates, M. E. & Poon, W. C. K. Migration of chemotactic bacteria in soft agar: Role of gel concentration. *Biophys. J.* **101**, 525–534 (2011).

[69] Elgeti, J., Winkler, R. G. & Gompper, G. Physics of microswimmers-single particle motion and collective behavior: a review. *Rep. Prog. Phys.* **78**, 056601 (2015).

[70] Abe, T., Nakamura, S. & Kudo, S. Bioconvection induced by bacterial chemotaxis in a capillary assay. *Biochem. Biophys. Res. Commun.* **483**, 277–282 (2017).

[71] Adler, J. Method for measuring chemotaxis and use of method to determine optimum conditions for chemotaxis by *Escherichia coli. J. Gen. Microbiol.* **74**, 77–91 (1973).

[72] Turner, L., Zhang, R. J., Darnton, N. C. & Berg, H. C. Visualization of flagella during bacterial swarming. *J. Bacteriol.* **192**, 3259–3267 (2010).

[73] Swiecicki, J. M., Sliusarenko, O. & Weibel, D. B. From swimming to swarming: *Escherichia coli* cell motility in two-dimensions. *Integr. Biol.* **5**, 1490–1494 (2013).

[74] Taute, K. M., Gude, S., Tans, S. J. & Shimizu, T. S. High-throughput 3D tracking of bacteria on a standard phase contrast microscope. *Nat. Commun.* **6**, 8776 (2015).

[75] Yang, Y. L. & Sourjik, V. Opposite responses by different chemoreceptors set a tunable preference point in *Escherichia coli* pH taxis. *Mol. Microbiol.* **86**, 1482–1489 (2012).
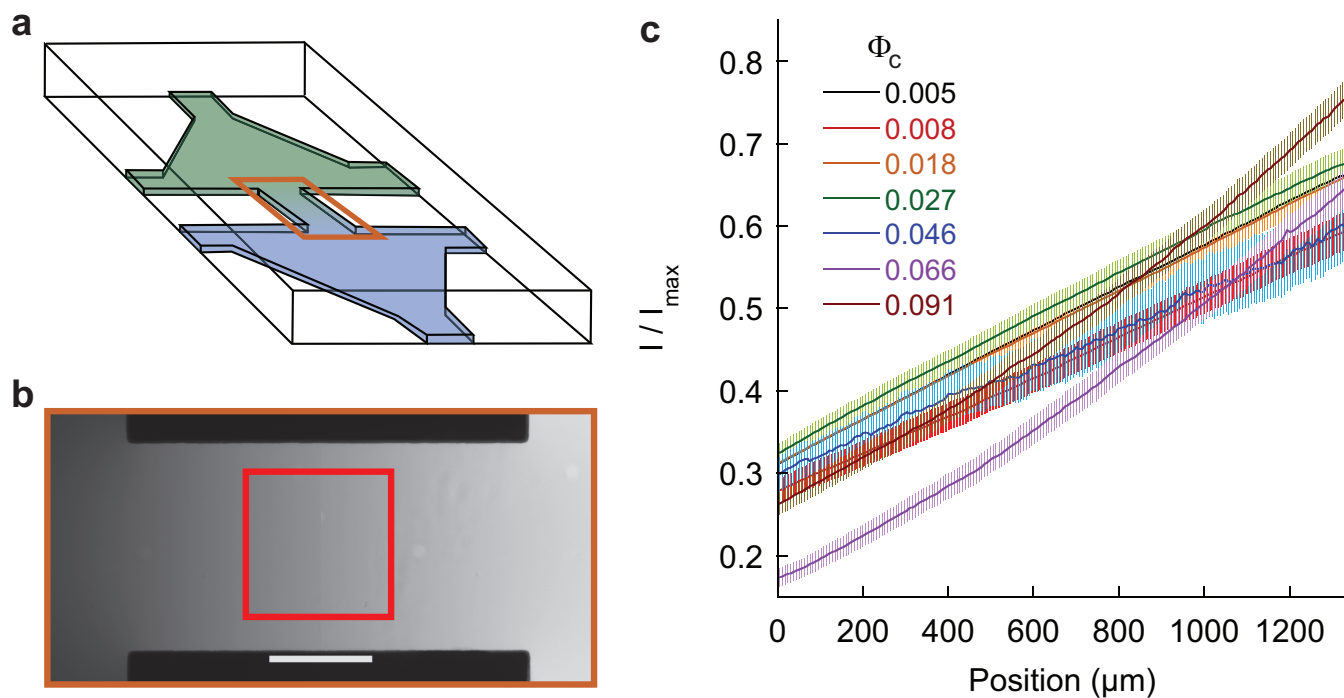
Fig. 1. Microfluidic device used for chemotaxis assays. **a,** Schematic representation of the device, where two reservoirs with different chemical composition are connected by a channel in which the chemoattractant gradient forms. **b,** Central part of the device, highlighted orange in (**a**), with gradient profile across the channel quantified using fluorescein. Scale bar is 500 μm. The red box indicates the location at which cellular behaviour is recorded. **c,** Examples of gradients, measured in the $h = 50\,\mu$m device, for cell suspensions of indicated cell densities. Error bars represent measurement error.
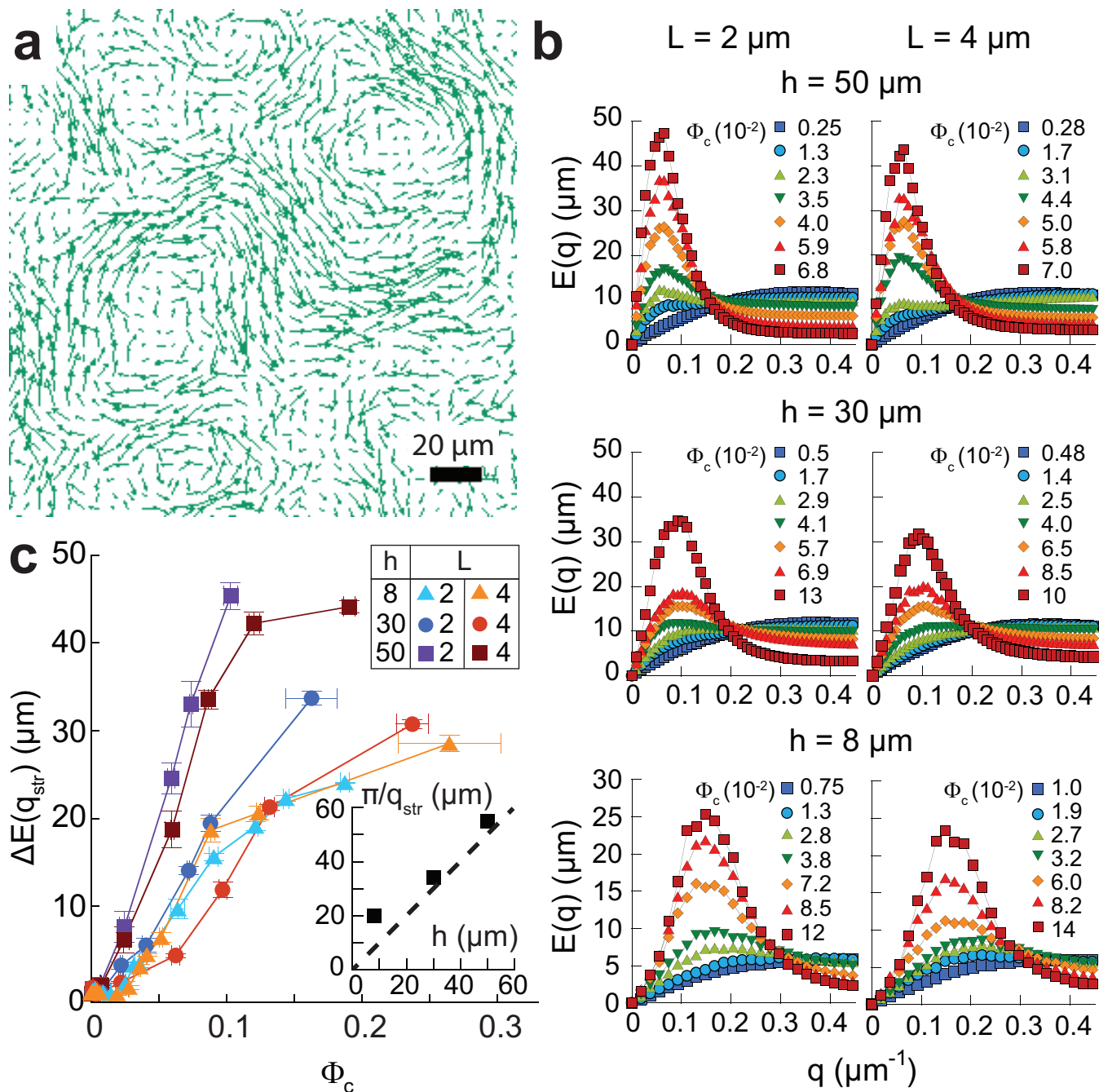
Fig. 2. Collective motion in bacterial suspensions. **a,** Typical snapshot of the velocity field measured in a high-density cell suspension ($\Phi_c = 0.08$, cell length $L = 2\,\mu$m, channel height $h = 50\,\mu$m). **b,** Flow structure factor $E(q)$ for increasing cell densities at the indicated values of channel height and cell length. **c,** Amplitude of the peak, corrected for the low density value, $\Delta E(q_{str})$ as a function of cell density in the different experimental conditions. Each point is the median, and associated error bar the standard error of the mean (SEM) of 8 measurements, binned according to cell density. Inset: π/q_{str} as a function of channel height. Dashed line indicates equality.
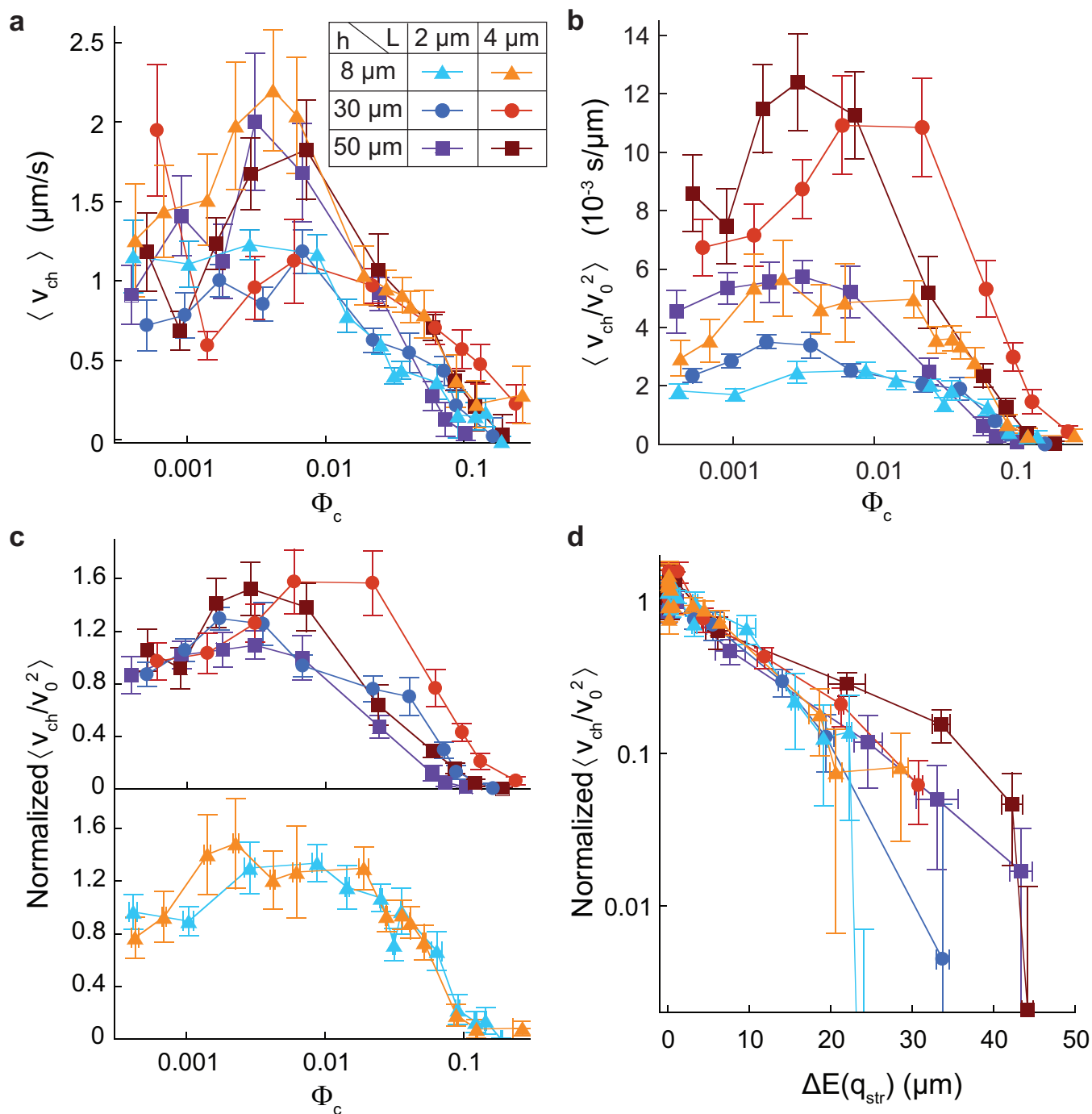
Fig. 3. Effect of collective motion on the chemotactic drift. **a,** Chemotactic drift v_{ch} as a function of cell density for indicated values of cell length (L) and channel height (h). **b,** Chemotactic coefficient v_{ch}/v_0^2 as a function of cell density. **c–d,** Chemotactic coefficient normalized to its low-density value as a function of cell density (**c**) or of the amplitude $\Delta E(q_{str})$ of the collective motion (**d**). Labels throughout the figure are defined in panel (**a**). Each point represents the median of 8 experiments. Error bars represent the SEM in abscissa and the sum of the SEM and the mean measurement error in ordinate.
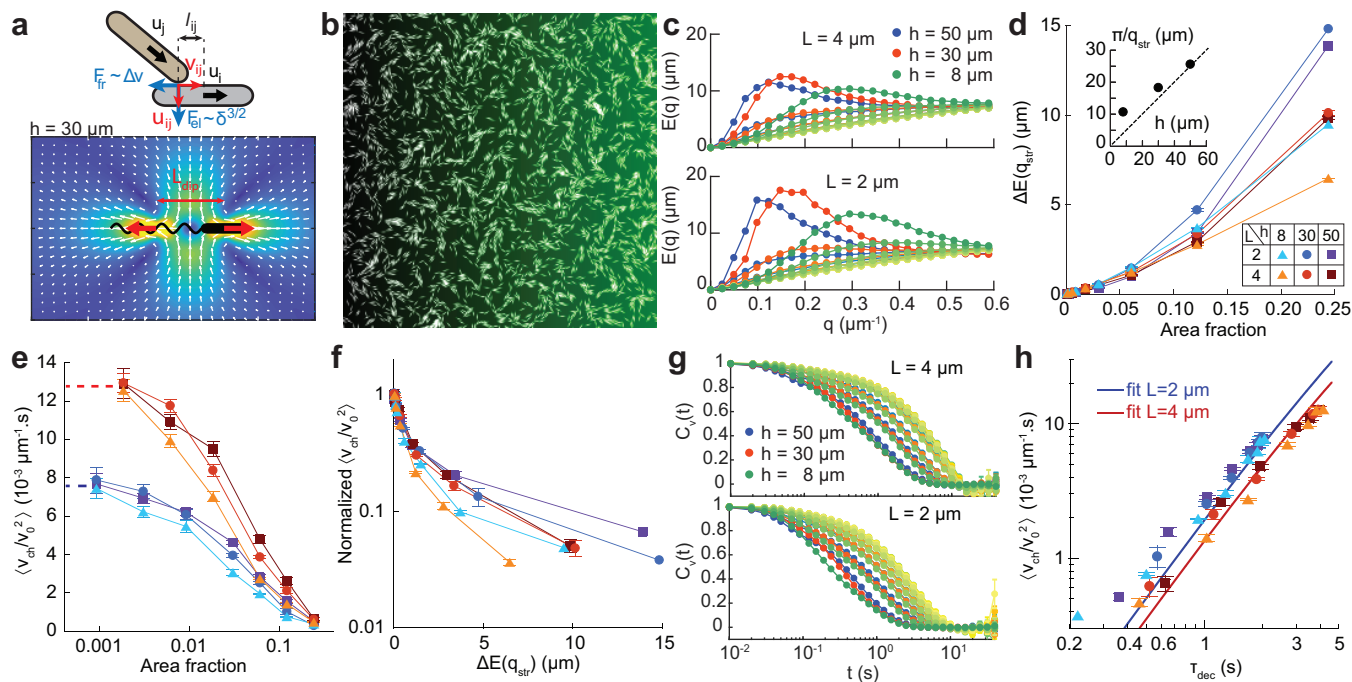
Fig. 4. Numerical simulations of self-propelled interacting chemotactic rods in 2D. **a,** Schematic representation of the simulated steric interaction between the rods, where interpenetration (δ) results in Hertzian-like repulsion (F_{el}) and friction (F_{fr}), and the fluid flow generated by the hydrodynamic force dipole, here for channel height $h = 30\,\mu$m. For other heights, see Supplementary Fig. 6. **b,** Snapshot of a simulation output (length $L = 4\,\mu$m, $h = 30\,\mu$m, $\Phi = 0.244$), showing collective motion of packs of rods. The green shading represents the gradient. **c,** Flow structure factor $E(q)$ for indicated conditions, exhibiting a growing maximum at a q_{str} depending only on the channel height h. Darkening shading of a given color indicates increasing area fraction in the range $0.002 - 0.25$. **d,** Maximum subtracted of its low density value, $\Delta E(q_{str})$, as a function of cell area fraction. (Inset) Typical vortex size π/q_{str} as a function of the channel height. Note the difference in scale compared to Fig. 2c. **e,** Chemotactic coefficient as a function of the cell area fraction. Dotted lines represent its value in absence of interactions. **f,** Chemotactic coefficient, normalized to its low density value, as a function of the maximum of the flow structure factor $\Delta E(q_{str})$. **g,** Time autocorrelations of the cells velocity, the color coding is the same as in panel **c**. **h,** Chemotactic coefficient as a function of the decorrelation time τ_{dec}, defined by $C_v(\tau_{dec}) = 0.5$, and fit according to Eq. 4. **d-f,h,** Conditions are as indicated in panel **d** and error bars represent SEM on at least 3 runs, totalizing at least 1000 cells.

22

649

Supplementary Information

650

Chemotactic behaviour of *Escherichia coli* at high cell density

651

Colin *et al.*

Supplementary notes

Supplementary Note 1. Peclet number

The Peclet number compares diffusion and advection of the chemical attractant in the fluid. It is defined as $Pe = hv_f/D$, since the typical size of the flow scales with the height of the channel. Here v_f is the velocity of the fluid. It can be estimated from the difference between the high density collective velocity and the free swimming speed assumed by the cell at low density. It never exceeded $10\,\mu$m/s (Supplementary Fig. 1). Taking the maximal $h = 50\,\mu$m, and considering that $D = 500\,\mu$m^2/s, leads to $Pe \leq 1$ for all experiments, no matter how strong the collective motion is. $Pe = 1$ indicates that distortions of the gradient are to be expected, as we observe in the case of the strongest collective motion.

Supplementary Note 2. Chemotactic drift in shallow gradients

Model of the pathway – The chemotaxis pathway of *E. coli* is composed of a large superstructure (array) of coupled receptor dimers, embedded in the inner membrane of the cell, and coassembled with the cytoplasmic kinase CheA and adaptor protein CheW. The most aboundant chemoreceptors of *E. coli* are Tar (the main sensor of MeAsp) and Tsr. Chemoeffectors bind the receptors on their periplasmic domain, inducing conformational changes which cooperatively modify the autophosphorylation activity of the kinase CheA, attractants reducing kinase activity. The cooperative array organization enables to integrate and amplify signals from different receptors. The kinase then transmits its phosphates to the small diffusible molecule CheY. Phosphorylated CheY binds to the motor to induce tumbles and is dephosphorylated by CheZ. The previous reactions are subsecond so that a sudden increase in attractant concentration induces a fast drop in the probability of tumbling. Two enzymes, CheR and CheB, then respectively add and remove methyl groups to specific amino-acids of the respectively inactive and active chemoreceptors in few seconds. This slowly offsets chemoeffectors action, adapting the average kinase activity – and thus the tumbling rate – back to the intermediate value it assumes in homogeneous environments, so that subsequent stimulations can be sensed. The current methylation level of the chemoreceptors then acts as a physical memory which represents the environment experienced by the cell a few seconds before, with which the current situation is compared.

We recall here the model of the chemotaxis pathway constructed in [59]. The chemoreceptor dimers were modeled as two-state variables interacting following a Monod-Wyman-Changeux allosteric model. The probability P_{on} of a signaling team of N_{a} Tar and N_{s} Tsr receptor dimers (and associated kinases) to be active is given by the free energy difference F between the active and inactive states as:

$$P_{\mathrm{on}} = \frac{1}{1 + e^F} \tag{21}$$

with the free energy difference:

$$F = (N_{\mathrm{a}} + N_{\mathrm{s}})\,\epsilon(m) + N_{\mathrm{a}} \ln\left(\frac{1 + c/K_{\mathrm{a}}^{\mathrm{off}}}{1 + c/K_{\mathrm{a}}^{\mathrm{on}}}\right) + N_{\mathrm{s}} \ln\left(\frac{1 + c/K_{\mathrm{s}}^{\mathrm{off}}}{1 + c/K_{\mathrm{s}}^{\mathrm{on}}}\right), \tag{22}$$

where K_i^{off} (resp. K_i^{on}) is the binding affinity of the chemoattractant, present at concentration c, to the receptor i in its inactive (resp. active) state. The methylation dependent free energy difference $\epsilon(m)$ is

24

linear by part, and defined as:

$$\epsilon(m) = \begin{cases} 1.0 - 0.5\,m, & 0 < m < 2 \\ -0.3\,(m - 2.0), & 2 < m < 4 \\ -0.6 - 0.25\,(m - 4.0), & 4 < m < 6 \\ -1.1 - 0.9\,(m - 6.0), & 6 < m < 7 \\ -2.0 - (m - 7.0), & 7 < m < 8 \end{cases} . \tag{23}$$

The methylation enzyme CheR methylates only inactive receptors with average rate k_R, and CheB demethylates only active ones with average rate k_B, so that the methylation level evolves according to:

$$\frac{\mathrm{d}m}{\mathrm{d}t} = k_R(1 - P_{on}) - k_B P_{on} \tag{24}$$

The previous set of equations makes the fraction of active teams P_{on} evolve in time, responding and adapting to the history of concentrations experienced by the cell $c(t)$. The balance between autophosphorylation of active kinases and phosphotransfer to CheY sets the fraction of phosphorylated CheA dimers A_p as:

$$A_p = \frac{k_A\,P_{on}}{k_A\,P_{on} + k_Y} . \tag{25}$$

Finally, the fast phosphorylation – dephosphorylation cycle of CheY sets the fraction of phosphorylated CheY as:

$$Y_p = 19.3610 \frac{k_Y\,A_p}{k_Y\,A_p + Z} . \tag{26}$$

If the cells are in the run state, the probability to tumble during the time step δt is given by:

$$p_{r \to t} = \exp\left(-\delta t\,(Y_p)^H / \tau_r\right) \tag{27}$$

If the cell is in a tumbling state, the probability to start running again is however independent of the CheY phosphorylation level:

$$p_{t \to r} = \exp\left(-\delta t / \tau_t\right) \tag{28}$$

All parameter values are given in Supplementary Table 2 and are as in [59] except for N_a and N_s which were chosen to match the values expected at the OD_{600} to which our cells are grown [75].

Prediction for the chemotactic drift in shallow gradients – We write here in our notations the results of Dufour *et al.* [51]. From Eq. 3 of this paper, because our simulations are 2D and the adapted value of Y_p is 1, we have:

$$v_{ch} = (1 - TB)v_0^2 N_a \nabla f(c)/2 \frac{\partial \ln \tau_{dec}}{\partial F} \frac{1}{1/\tau_R + 1/\tau_T + 1/\tau_m} \tag{29}$$

were $(1 - TB) = \tau_r/(\tau_t + \tau_r)$ is the fraction of running cells at any given time in absence of a gradient, $\tau_m = 0.5(N_s + N_a)P_{on}(1 - P_{on})(k_R + k_B)$ is the relaxation time of F according to Eq. 22 and 24, $1/\tau_{dec} = 1/\tau_R + 1/\tau_T$, and the derivative is taken at the adapted value $F = \ln 2$. We have also defined the Brownian reorientation time $\tau_R = 1/D_r$, and the tumbling reorientation time $\tau_T = \tau_r(Y_p)^{-H}/(1 - \exp(-D_T \tau_t))$. The latter accounts for the incomplete randomization due to finite tumbling time [52], which was not accounted for in Dufour *et al.* [51] because complete randomization was assumed. We now considere that:

$$\frac{\partial \ln \tau_{dec}}{\partial F} = -\tau_{dec} \frac{\partial (Y_p)^H}{\partial F}(1 - \exp(-D_T \tau_t))/\tau_r = -H \frac{\tau_{dec}}{\tau_T} \frac{1}{Y_p} \frac{\partial Y_p}{\partial F} \tag{30}$$

25

We also have from Eq. 21, 25 and 26 that:

$$\frac{1}{Y_{\mathrm{p}}}\frac{\partial Y_{\mathrm{p}}}{\partial F} = -(1 - \frac{k_{\mathrm{Y}}A_{\mathrm{p}}}{k_{\mathrm{Y}}A_{\mathrm{p}} + Z})(1 - \frac{k_{\mathrm{A}}P_{\mathrm{on}}}{k_{\mathrm{A}}P_{\mathrm{on}} + k_{\mathrm{Y}}})(1 - P_{\mathrm{on}}) \simeq -(1 - P_{\mathrm{on}}) \tag{31}$$

since the other factors are very close to 1, when one considers that they have to be evaluated for $F = \ln 2$. We then have:

$$v_{\mathrm{ch}} = v_0^2 (1 - TB)N_{\mathrm{a}}H(1 - P_{\mathrm{on}})/2\frac{\tau_{\mathrm{R}}}{\tau_{\mathrm{R}} + \tau_{\mathrm{T}}}\frac{1}{1/\tau_{\mathrm{R}} + 1/\tau_{\mathrm{T}} + 1/\tau_{\mathrm{m}}}\nabla f(c) \tag{32}$$

which corresponds to Eq. 2 (and equivalently 4) of the main text, with the coefficients given in Supplementary Table 2.

Supplementary Note 3. Chemotactic behavior in simulations in absence of hydrodynamic interactions

Supplementary Fig. 7 shows the main characteristics of the collective motility and the drift in the simulations where hydrodynamic interactions are neglected. Note that the rotational Brownian motion was also neglected. The characteristics of the collective motion, as measured by the flow structure factor $E(q)$, were set by the cell length L (Supplementary Fig. 7**b-d**). The chemotactic drift first decreased with area fraction, before increasing, peaking and decreasing again for $L = 3\,\mu$m and $4\,\mu$m (Supplementary Fig. 7**e**). Contrary to the experiments, there was no scaling with $E(q_{\mathrm{str}})$ (Supplementary Fig. 7**f**).

Interestingly, the velocity decorrelation time τ_{dec} extracted from the time autocorrelation of the single cell velocity (Supplementary Fig. 7**g**) decreased monotonously in all conditions as a function of area fraction (Supplementary Fig. 10**a**), as it did when hydrodynamics was accounted for. However, in the dry case, the chemotactic coefficient, considering its dependence in τ_{dec}, did not follow Eq. 4 of the main text (Supplementary Fig. 7**h**), contrary to the full simulations (main Fig. 4**h**). Clearly, at the densities were the drift started to reincrease, the system started to depart from the framework of Eq. 4 of the main text, which assumes a Brownian motion like reorientation process and shallow gradients, i.e. that the average pathway activity P_{on} departs only slightly from its adapted value. Because it occurs at a fairly high cell density, it is however not clear if the peak observed here occurs for the same reasons as the one observed in the experiments.

Supplementary Note 4. Dual effect of physical interactions on the chemotactic drift

An extension of the model we used so far to explain chemotactic drift reduction (i.e. [51] leading to Eq. 2-4 of the main text) was proposed in Long *et al.* [54]. There, this extension was used to explain non-linear reinforcement of the chemotactic drift when the gradient is sharp enough. It therefore does not assume shallow gradients anymore, and is based on a Schmolukovski equation for the space-averaged probability $P(t, F, s)$ to be at time t with a chemoreceptor free energy F and an orientation $s = \mathbf{n} \cdot \nabla c/||\nabla c||$ [54]:

$$\partial_t P = -\partial_F \left(\left(-(F - F_0) + \frac{r(F)s}{H\tau_{\mathrm{E}}} \right) P \right) + \frac{\hat{L}_s P}{\tau_D(F)} . \tag{33}$$

Here time is normalized to the adaptation time τ_{m} and $r(F)$ is the probability of the cell being running, given the receptor free energy F. The first right hand side term describes the chemoreceptor free energy actuation

26

739 according to adaptation (term $-(F - F_0)$ with F_0 the adapted, unstimulated, value of F; $F_0 = \ln 2$ in our
740 case) and stimulation due to swimming in the gradient (with $1/H\tau_E$ being the normalized gradient, defined
741 in Supplementary Table 2 for our case). The second term describes reorientations due to Brownian rota-
742 tional diffusion and tumbles, with $\hat{L}_s$ the rotational diffusion operator and $\tau_D = 1/(\tau_m(rD_r + (1 - r)D_T))$
743 comparing reorientation and adaptation times. Assuming that the detailed balance in the angular fluxes of
744 cell orientation hold, we can include in this second term the effect of collective reorientations in the form
745 of an effective enhanced rotational diffusion $D_r \to D_r + D_{coll}^{eff}$. Integrating this equation over orientations,
746 in Long *et al.* [54] it is shown that at steady state in the gradient:

$$v_{ch}/v_0 = \langle rs \rangle = H\tau_E \langle F - F_0 \rangle \tag{34}$$

747 Here the chemotactic ratio v_{ch}/v_0 is the product of the normalized gradient strength and of the average
748 over all positions, orientations and times of the shift in chemoreceptor free energy from its adapted value
749 (CFES, $\langle F - F_0 \rangle$). Key assumptions for derivating this equation are steady-state and detailed balance
750 holding. In this equation, the effect of reorientations (tumbles, Brownian motion and possibly collective
751 reorientations) on the drift is accounted for by a reduction of the CFES. In the simulations (contrary to
752 experiments), the CFES is readily accessible, and it evolves similarly to the drift as a function of volume
753 fraction (Supplementary Figs. 9**b** and 10**b**). The chemotactic ratio v_{ch}/v_0 follows Eq. 34 as a function of
754 $\langle F - F_0 \rangle$ fairly well in the simulations accounting for hydrodynamics (Supplementary Fig. 9**c**), but less so
755 for the dry simulations (Supplementary Fig. 10**c**). Upon closer inspection using the ratio

$$\frac{v_{ch}/v_0}{H\tau_E \langle F - F_0 \rangle} \tag{35}$$

756 we find that the ratio decreases in both cases below 1 when collective reorientations increase, as measured
757 by the decrease of the decay time of the autocorrelation of the cell velocity, τ_{dec} (Supplementary Figs. S9**d**
758 and S10**d**). This deviation from Eq. 34 is weaker when hydrodynamics is included. Since we ensured that
759 steady state is reached (in 1000 frames, 10 s of real time equivalent) before measuring the averages, we
760 deduce that this discrepancy must come from detailed balance in the angular fluxes not being respected.
761 Indeed, detailed balance assumes that:

$$P(s)\phi(s \to s + ds) = P(s + ds)\phi(s + ds \to s) \tag{36}$$

762 where $\phi(s \to s + ds)$ is the flux of cells changing their orientation from s to $s + ds$ over a small amount
763 of time, and it is not necessarily satisfied when hydrodynamics- and collision-induced reorientations are
764 concerned. Indeed, vortices are a net flux of orientation which thus cannot satisfy Eq. 36. Therefore, when
765 hydrodynamics is included and even more so in the dry simulations, the effect of cell-cell interactions is
766 not fully comparable to Brownian motion (for which detailed balance holds), and we prefer in this sense to
767 talk about active enhancement of rotational diffusion, where $H\tau_E \langle F - F_0 \rangle$ represents the drift if detailed
768 balance was holding, and the ratio (35) is a measure of the effect of detailed balance breakdown.

27
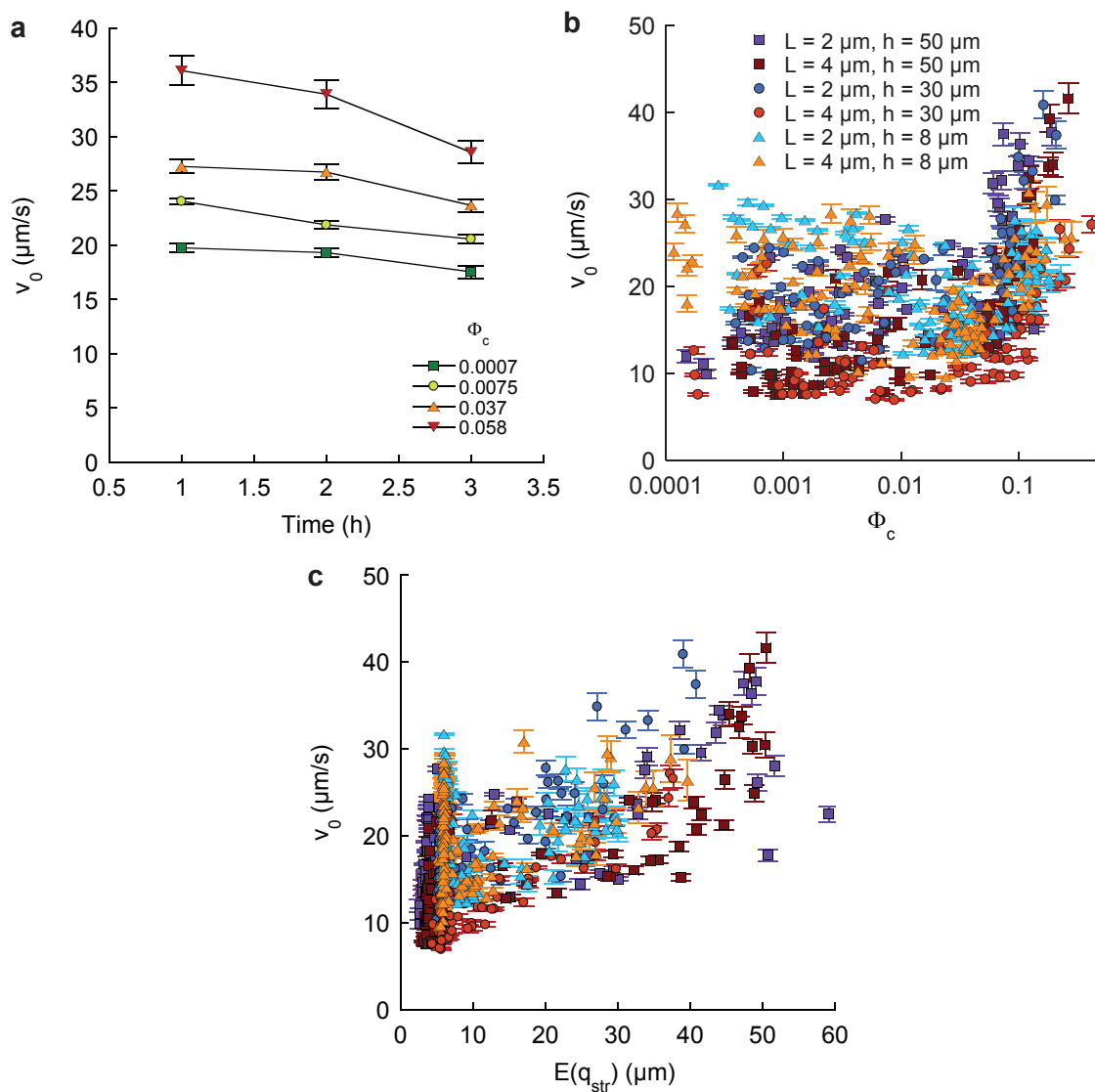
Supplementary Figure 5. (**a**) Examples of average swimming speed as a function of the time since sample preparation for normal cells in 50 μm high channels at indicated cell densities. The experiments were performed during the first three hours, for which swimming speed is fairly constant. (**b**) Average swimming speed, for all individual measurements, plotted as a function of cell body volume fraction. (**c**) The swimming speeds for all conditions were function of the amplitude of the collective motion, as defined in the main text, at high cell density. (**b-c**) Error bars represent measurement error.
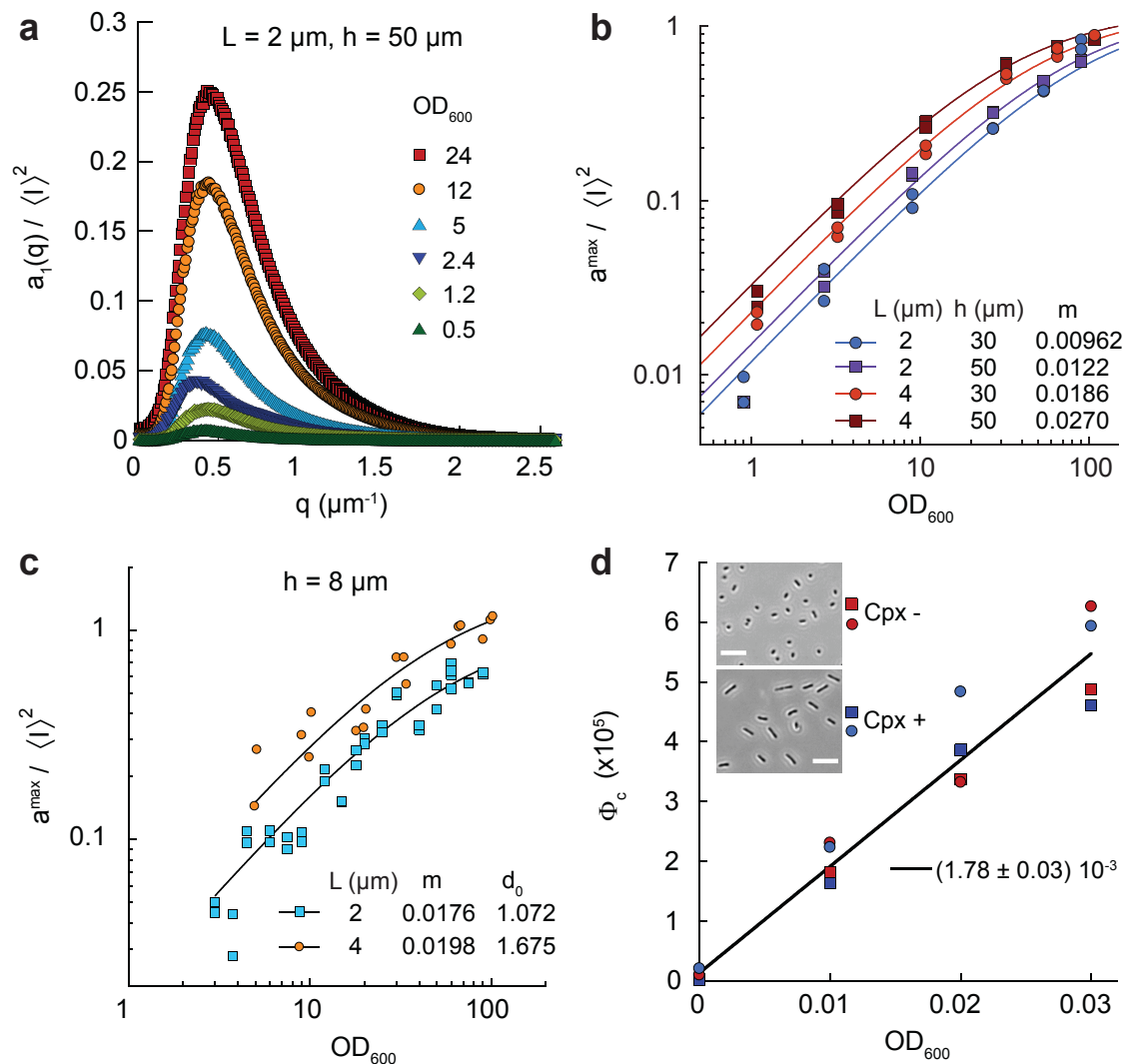
Supplementary Figure 6. *In situ* calibration of the cell body volume fraction. (**a**) The normalized amplitude of the differential intensity correlation function a_1/I^2, measured here in chemically homogeneous microfluidic devices, exhibits a maximum as a function of the spatial wave number q, which increases with the optical density. (**b**) The maximum value of a_1/I^2 can be fitted as $a_1^{\max}/I^2 = 1.25\, m\, \mathrm{OD}_{600}/(1 + m\, \mathrm{OD}_{600})$, with m depending on cell length L and channel height h, indicated in μm. (**c**) For channel height $h = 8\,\mu$m, the better adapted formula $a_1^{\max}/I^2 = d_0\, m\, \mathrm{OD}_{600}/(1 + m\, \mathrm{OD}_{600})$ was used. (**d**) The cell body volume fraction Φ_c was calibrated as a function of optical density for the single spectrophotometer used in the study, by cell counting in flow cytometry and length measurement in microscopy. The optical density was a single linear function of Φ_c, irrespective of cephalexin treatment. (Inset) Typical phase contrast images for cell length measurements, with and without cephalexin (Cpx) treatment. Scale bars are $10\,\mu$m.
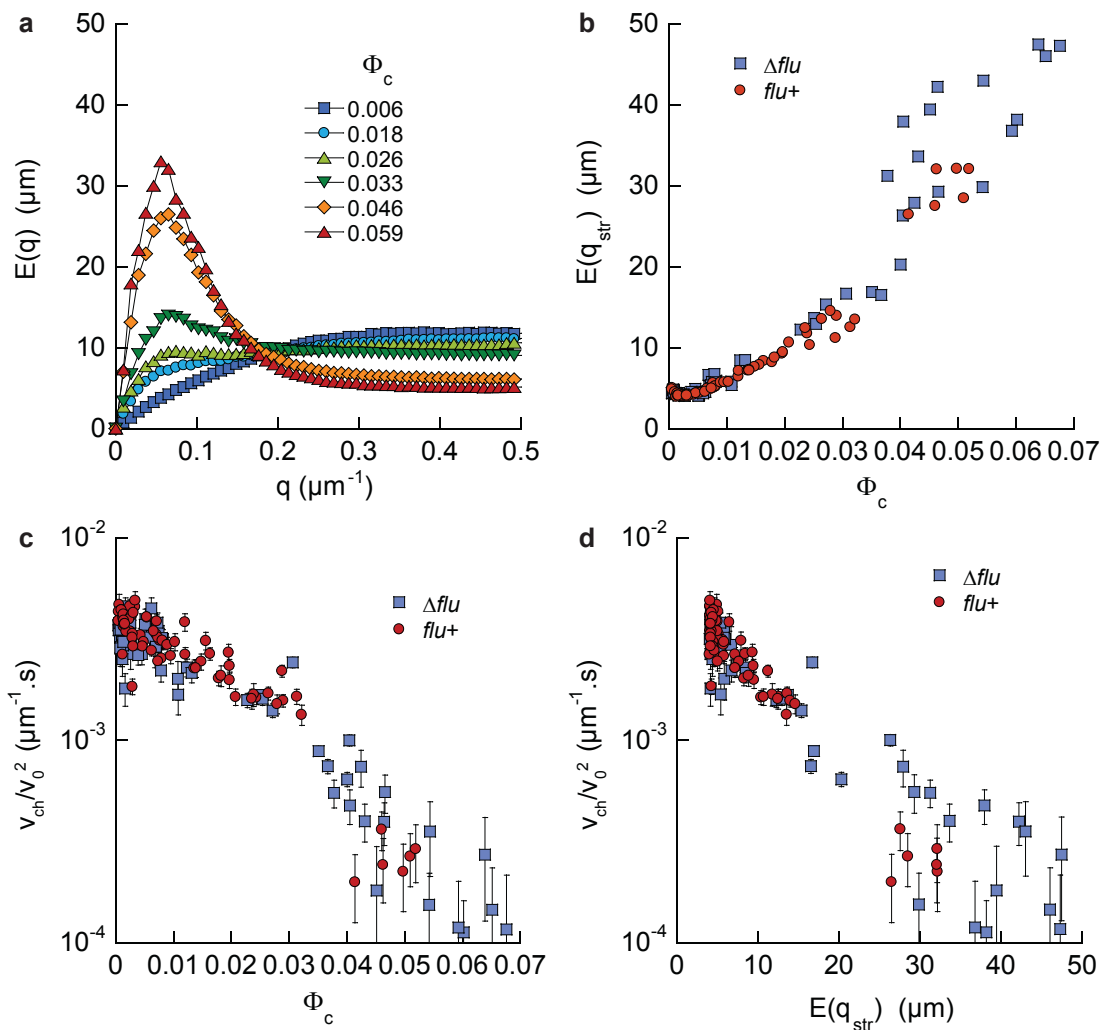
Supplementary Figure 7. Comparison of the behavior of $flu+$ and Δflu cells. (**a**) The spatial power spectral density E(q) measured in the $50\,\mu$m high channels exhibited a peak at $\pi/q_{str} = 50$ μm, as in the Δflu mutant, growing with cell density. (**b**) The maximum value of E(q) grew in exactly the same manner for both strains. (**c-d**) The normalized chemotactic drift had the same dependence on the cell body volume fraction (**c**) and on the amplitude of the collective motion E(q$_{str}$) (**d**) in both strains.
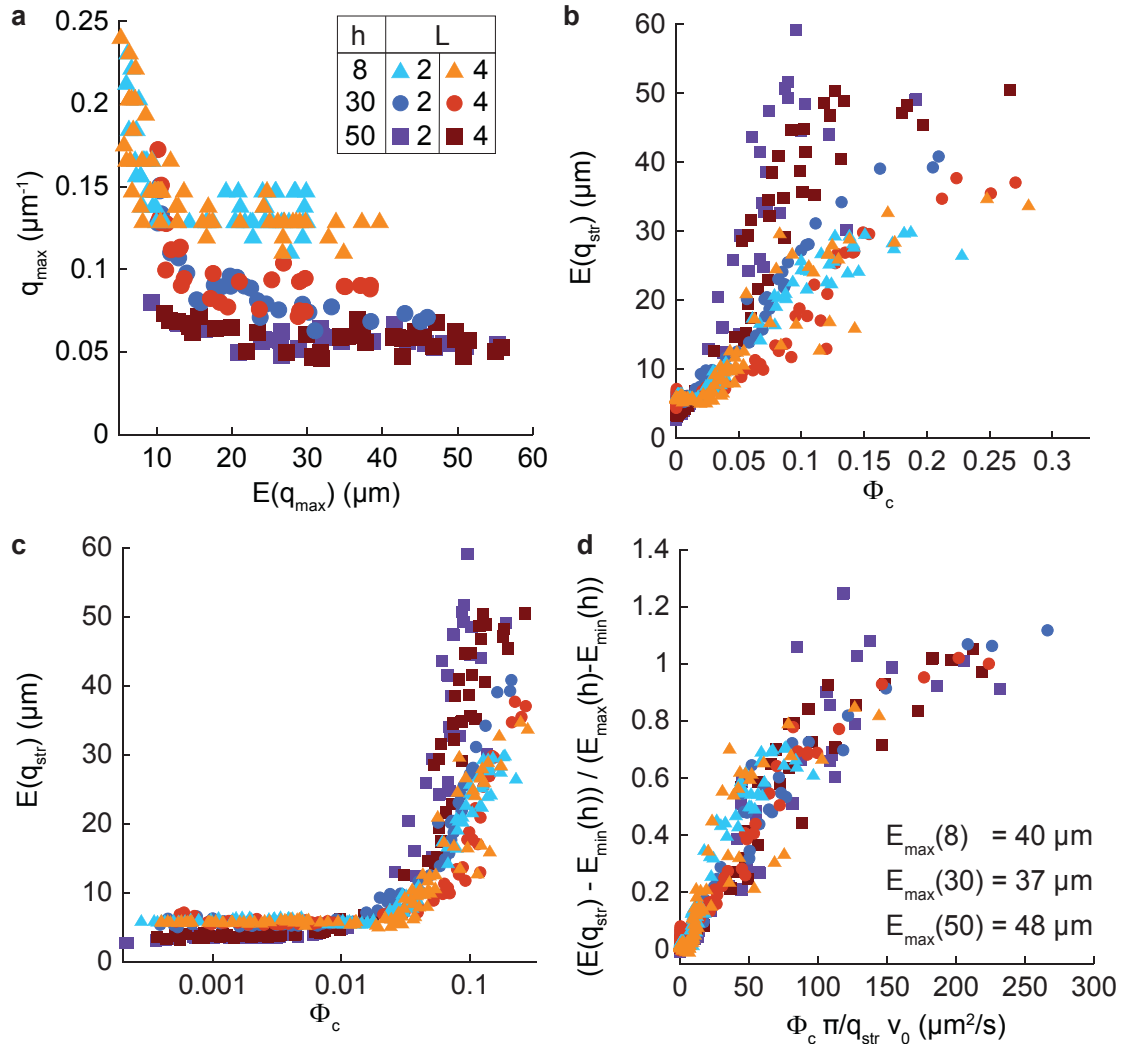
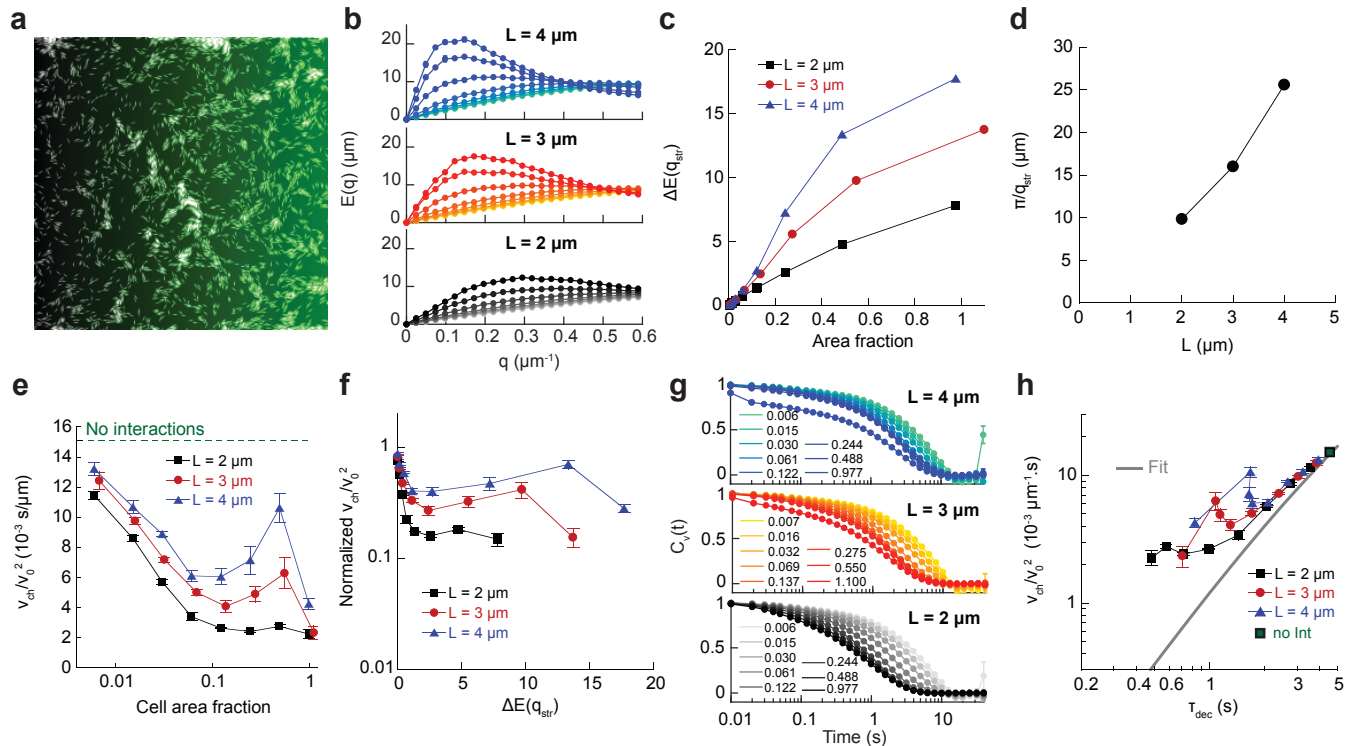**Supplementary Figure 8.** Supplemental analysis of the collective motion. (**a**) Wave number q_{max} for which the maximum of E(q) is reached as a function of this maximum $E(q_{max})$, for all conditions. When the amplitude of the collective motion as quantified by $E(q_{max})$ is high, q_{max} reaches a plateau at q_{str}, which depends in first approximation only on the height h of the channel. Each point represents a single experiment. (**b**) Amplitude $E(q_{str})$ of the collective motion, measured at the plateau wave number $q_{str}(h)$, for each individual experiments, and used to draw Fig. 2**c**. We used $q_{str}(8\,\mu m) = 0.15\,\mu m^{-1}$, $q_{str}(30\,\mu m) = 0.093\,\mu m^{-1}$ and $q_{str}(50\,\mu m) = 0.055\,\mu m^{-1}$. (**c**) Same as **b** with Φ_c in logarithmic scale. (**d**) $E(q_{str})$, when corrected for its low density value $E_{\min}(q_{str}(h))$ and normalized to the value at which it saturates at large density $E_{\max}(h)$, appears to be a single function of the cell body volume fraction times typical vortex size times swimming speed ($\Phi_c\,\pi/q_{str}\,v_0$).
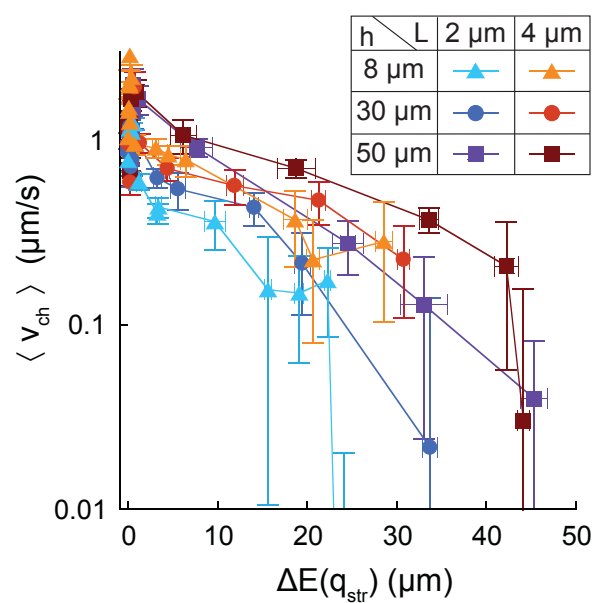
Supplementary Figure 9. Chemotactic drift v_{ch} as a function of the amplitude of the collective motion $\Delta E(q_{str})$. It decreases in all experimental conditions.
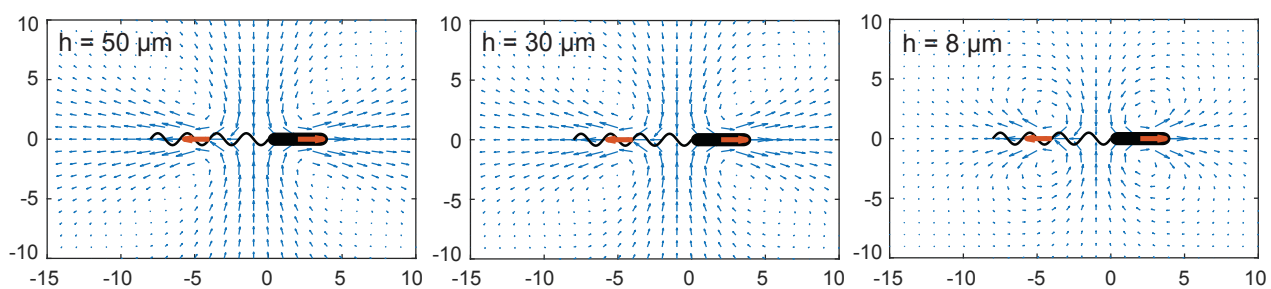
**Supplementary Figure 10.** Flow field generated around a swimmer for the three simulated heights.

Supplementary Figure 11. Numerical simulations of self-propelled chemotactic rods considering only steric interactions. (**a**) Snapshot of a simulation, with linear gradient imprinted in green (area fraction 0.244, $L = 4$). (**b**) Flow structure factor $E(q)$ for increasing volume fractions and indicated aspect ratios, showing a peak at q_{str} scaling with the aspect ratio. (**c**) Maximum $E(q_{str})$, subtracted of its low density value, as a function of cell area fraction. Note that contrary to experiments and the wet case, $E(q_{str})$ grows more slowly for shorter cells. (**d**) The typical size of the vortices depends on the cell aspect ratio, contrary to experiments and the wet case. (**e**) Chemotactic coefficient as a function of cell area fraction for the indicated aspect ratios. The green dotted line represents the value in absence of interactions. As in the experiments, it decreases and exhibit a peak for large aspect ratios. (**f**) Chemotactic coefficient as a function of the amplitude $E(q_{str})$. (**g**) Time autocorrelation of the cell velocity $C_v(t)$ for the indicated cell area fractions and aspect ratios. (**h**) Chemotactic bias v_{ch}/v_0 as a function of the normalized decorrelation time. The gray line represents the fit by Eq. 4 of the main text. The green dot represents the value in absence of all interactions.
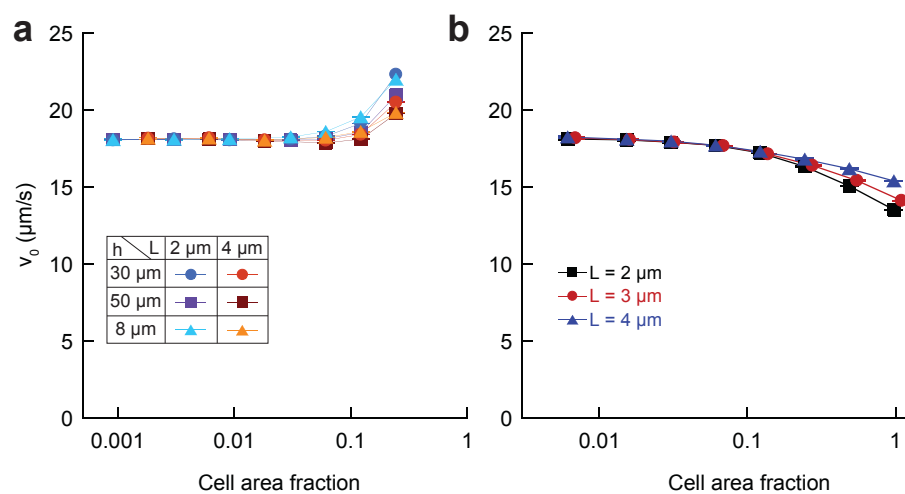
Supplementary Figure 12. Average swimming speed of the cells in the simulations in presence (**a**) or in absence of hydrodynamic interactions (**b**) as a function of cell volume fraction, for indicated cell lengths L, and channel heights h in the hydrodynamic case.
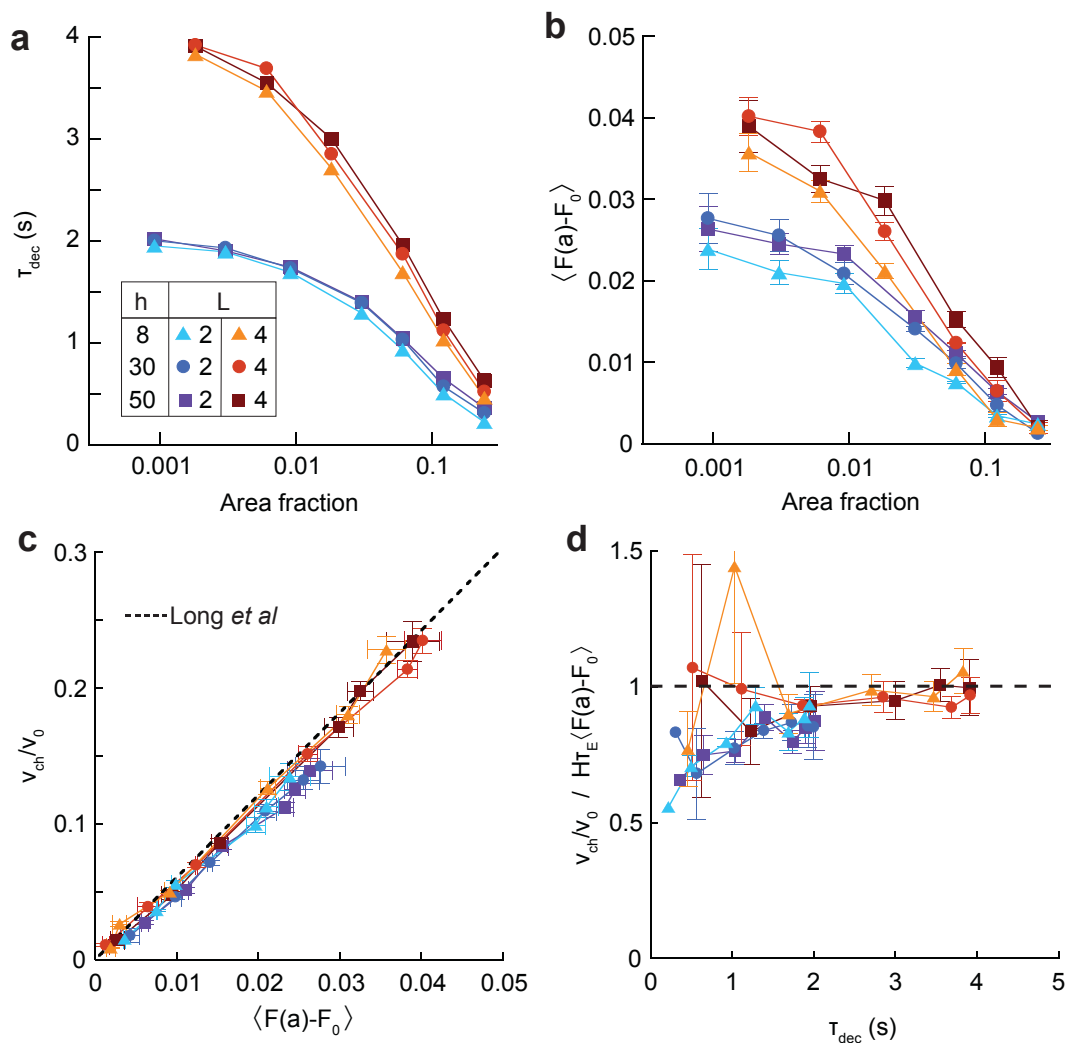
Supplementary Figure 13. Decorrelation time analysis in the simulations including hydrodynamics. (**a**) Decorrelation time, taken as $C_v(\tau_{\mathrm{dec}}) = 0.5$ for the indicated simulation parameters. (**b**) Chemoreceptor free energy shift (CFES) as a function of area fraction (**c**) The chemotactic bias as a function of the CFES. The dotted line is the prediction of Long *et al.* [54]. (**d**) The normalized bias divided by the CFES as a function of the decorrelation time.
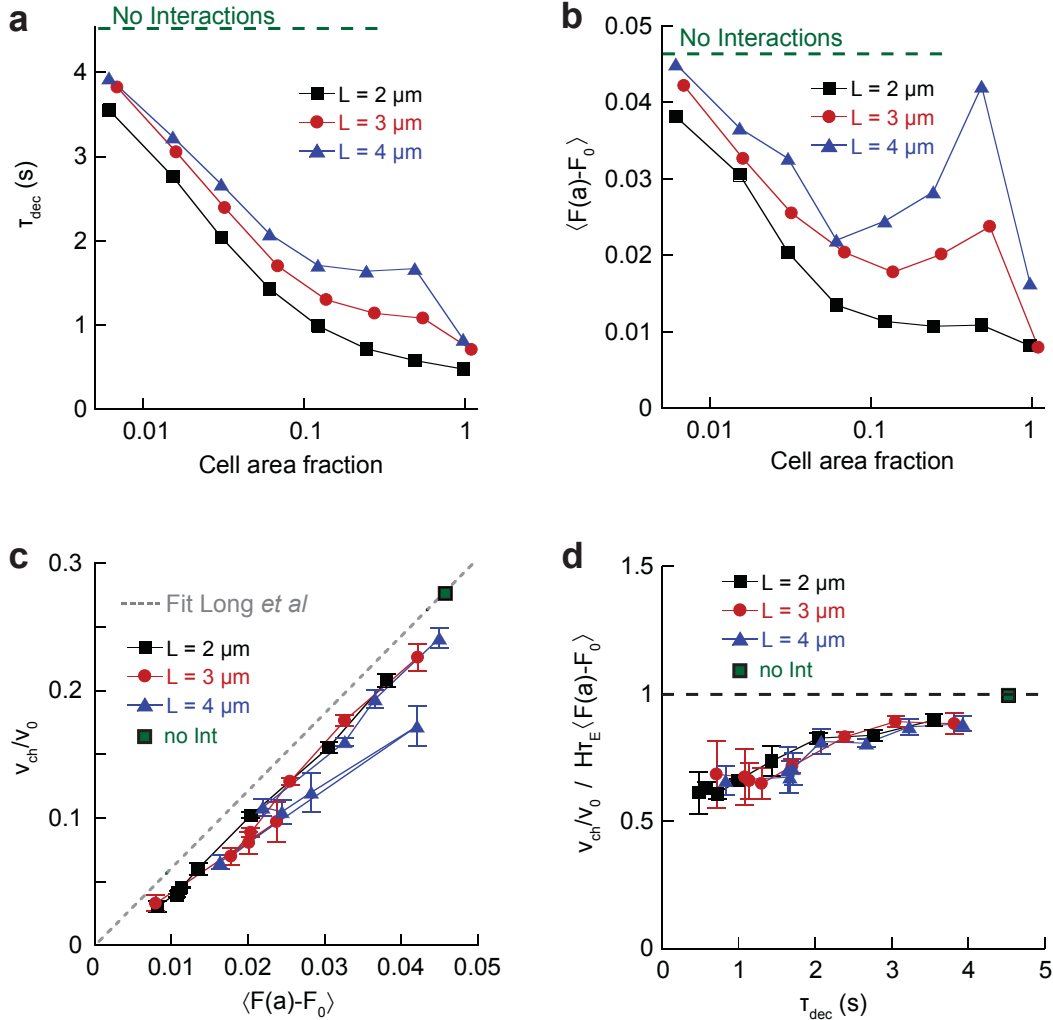
Supplementary Figure 14. Decorrelation time analysis in the dry simulations. (**a**) Cell velocity decorrelation time τ_{dec}, defined by $C_v(\tau_{dec}) = 0.5$ as a function of the area fraction. (**b**) The chemoreceptor free energy shift (CFES) is non monotonous as a function of area fraction. (**c**) Normalized chemotactic bias as a function of the normalized CFES. The gray dotted line represents the linear expectation from theory satisfying detailed balance [54]. (**d**) The normalized bias divided by the CFES, representing the fraction of the drift explainable assuming detailed balance is satisfied, as a function of the decorrelation time. (**a-d**) The green dotted line (**a-b**) or dot (**c,d**) represents the value in absence of all interactions.
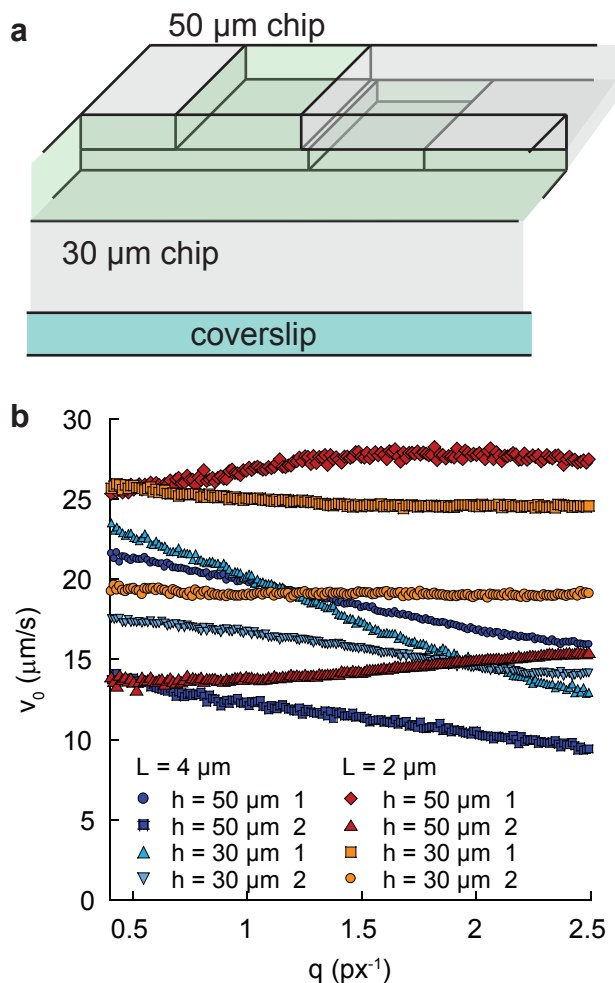
Supplementary Figure 15. Calibration of the velocity measurement by DDM. (**a**) Scheme of the geometry to compare DDM measurements of velocities in the 30 (or 8) μm and 50 μm devices. The two devices are facing each other and measurements can be done on the same suspension of cells in both channels. (**b**) Typical velocity outputs of the fit of the differential image correlation functions as a function of the wave number q, for the various experimental conditions. The effective velocity decreases for the longer cells, because of the anisotropy effect (see Supplementary note 5). The slight increase for the shorter cells was attributed to tumbles in earlier studies [46, 47].

769 **Supplementary Table 1**. Spincoating parameters

770

height (μm)	SU8	spincoat speed (rpm)
50	2050	1500
30	2050	3000
8	2015	2500

Supplementary Table 2. Parameters of the simulations

v_0	$20 \, \mu\text{m.s}^{-1}$
dv_0	$2 \, \mu\text{m.s}^{-1}$
δt	10^{-4} s
1 frame	10^{-2} s
$\nabla c/c_0$	$2 \, 10^{-4} \, \mu\text{m}^{-1}$
c_0	$10^2 \, \mu\text{M}$
Chemotaxis pathway	
τ_r	1 s
τ_t	0.1 s
H	10
N_a	10
N_s	10
K_a^off	$20 \, \mu\text{M}$
K_a^on	3 mM
K_s^off	1 mM
K_s^on	10 mM
k_R	0.0182 s^{-1}
k_B	0.0364 s^{-1}
Z	31
k_A	5
k_Y	100
Interaction parameters	
K_el/η	$10 \, \mu\text{m}^{1/2}.\text{s}^{-1}$
K_fr/η	$0.1 \, \mu\text{m}$

Cell parameters		
L	$2 \, \mu\text{m}$	$4 \, \mu\text{m}$
D_T	$6.7 \, s^{-1}$	$4.2 \, s^{-1}$
D_r	$0.1 \, s^{-1}$	$0.0125 \, s^{-1}$
L_flag	$10 \, \mu\text{m}$	$10 \, \mu\text{m}$

Modelisation parameters	
Gain G	$\tau_\text{r}/(\tau_\text{r} + \tau_\text{t}) \, H N_\text{a}(1 - P_\text{on})/2$
τ_m	$0.5(N_\text{s} + N_\text{a})P_\text{on}(1 - P_\text{on})(k_\text{R} + k_\text{B})$
$\nabla f(c)$	$\nabla c \left(1/(c_0 + K_\text{a}^\text{off}) - 1/(c_0 + K_\text{a}^\text{on})\right)$
τ_0	$\tau_\text{r}/(Y_\text{p})^H$
$1/H\tau_\text{E}$	$N_\text{a}\tau_\text{m}v_0\nabla c/c_0$